Journal of Bio- and Tribo-Corrosion (2023) 9:41
https://doi.org/10.1007/s40735-023-00765-6

A Comprehensive Review on Ceramic Coating on Steel and Centrifugal Thermite Process: Applications and Future Trends

U. V. Akhil[1] · N. Radhika[1] · L. Rajeshkumar[2] · Giribaskar Sivaswamy[3]

Received: 9 February 2023 / Revised: 12 April 2023 / Accepted: 28 April 2023 / Published online: 7 May 2023

Abstract

Steel substrates used in high-pressure applications or when subjected to extreme environments have the drawback of corroding and eroding. Extensile studies have been done related to ways to protect the surface with different types of coating, considering the downtime and extra costs associated with maintenance. Ceramic coating over steel surfaces has been extensively researched as it provides a practical solution for using steel in extreme working conditions with enhanced high-temperature oxidation resistance. Nowadays, numerous methods for applying ceramic coatings over steel substrates were explored and can be selected based on the characteristics of the substrate, the type of coating material, and the desirable characteristics of the coating. Recent research focuses on fine-tuning coating qualities for high-end applications, by adding additives, and optimizing process parameters to improve coating properties. In this review, the fabrication methods adopted for ceramic coatings over steel, as well as their microstructural characteristics, applications, and potential future trends, are presented and discussed.

Keywords Plasma spray · Ceramics · Centrifugal thermite · Laser cladding · Wear · Corrosion

1 Introduction

Steels are among the engineering alloys that are most frequently used in industries, mostly because of their favourable characteristics, such as high toughness, tensile strength, machinability, and low processing cost. In spite of being mostly used, it also has certain demerits like oxidation, erosion, corrosion, and scaling. The petroleum sector has been dealing with a growing amount of pipeline corrosion and erosion, particularly in H_2S environments. Due to the unpredictable nature of stoppages and the high maintenance costs, erosion, wear, and corrosion problems can be expensive, and the associated downtime has a detrimental effect [1]. Corrosion reduces the mechanical properties of the materials while the corrosion products are discharged in various ways that may result in a more intensive corrosive environment or adverse side effects in various applications [2]. Thermal power plants receive Indian non-coking coal that contains up to 40% ash, the ash contains a significant amount of (abrasive/erosive) quartz. Thermal power stations produce a significant amount of fly ash/bottom ash, which is then dumped into ash ponds as a (water-ash) slurry which shortens the pipelines' lifespans due to erosion. A minor part rupturing could need the urgent replacement of entire systems and may result in long-term harm to people and the environment. This calls for the usage of pipes, tubes, and other similar parts, all of which have resistance against (slurry) erosion and abrasion. Similar issues arise when water is sprayed upon coal slurry in thermal power generation businesses [3]. The major conduits for fluid flow in thermal recovery

✉ N. Radhika
n_radhika1@cb.amrita.edu

U. V. Akhil
cb.en.p2mfg21001@cb.students.amrita.edu

L. Rajeshkumar
lrkln27@gmail.com

Giribaskar Sivaswamy
giribaskar.sivaswamy@strath.ac.uk

[1] Department of Mechanical Engineering, Amrita School of Engineering, Amrita Vishwa Vidyapeetham, Coimbatore, India

[2] Department of Mechanical Engineering, KPR Institute of Engineering and Technology, Coimbatore 641407, Tamilnadu, India

[3] Advanced Forming Research Centre (AFRC), University of Strathclyde, 85 Inchinnan Drive, Renfrew, Glasgow, Scotland, UK

wells are the downhole casing and tubing. Wall thinning, deformation, fracture, and corrosion of casing and tubing in high-pressure and high-temperature fluid can lead to string failure [4]. Since geothermal systems contain a variety of aggressive ingredients such as salt brines, hydrogen chloride (HCl), hydrogen sulphide (H_2S), and carbon dioxide (CO_2) gas from volcanic systems, corrosion, and erosion can be a major problem for components used in power plants. Pressure, temperature, pH, and other factors may also lead to corrosion and erosion in geothermal power plants [5, 6]. The combined mechanical and chemical interaction of erosion or abrasion with corrosion is to blame for severe damage and substantial losses that occur to equipment in various slurry transportation and handling processes, it has become increasingly obvious in the oil business. When exposed to an erosive environment, stainless steel (SS) becomes more susceptible to pitting corrosion [7]. Different approaches, including heat treatment, alloying procedures, and coatings, have been proposed to address these problems and improve the material properties. Since coating layers can cut costs and ignore material scarcity due to their thickness rarely exceeding micrometres, coating procedures among these have the largest percentage of material augmentation. As a result, fewer elements are required to build coating on a significant area of the substrate. Coatings can provide a variety of characteristics, including improved surface hardness, altered surface roughness, thermal and electrical insulation properties, increased wettability, and others [8–10]. Due to the diversity of applications and needs in various industries, different coating technologies are widely available. These procedures involve a wide range of online and offline parameters and result in a wide range of material microstructure, efficacy, appropriateness, and durability. However, coating techniques are beneficial in specific applications depending on the desired functionality, the most important of which being corrosion and wear protection [11]. The choice of materials is the most important factor in creating a successful coating, as they serve all protective functions. To create a protective layer, a variety of substances, such as metals, ceramics, and polymers, can be employed [12, 13]. Enhancing the mechanical performance of metallic substrates has always been possible by covering the metal surfaces with a thin ceramic layer, as ceramic coatings offer better resistance to corrosion, erosion, and provide high-temperature stability. There are numerous ceramic coating techniques currently available for the application of protective ceramic coatings. The achieved coating quality, deposition effectiveness, process complexity, and investment costs of these approaches vary [14–16]. Successive various studies reported over the past 10 years have been shown in Fig. 1. This review paper acquaints comprehensive insights on the ceramic coating on steel with subsequent sections of this paper reviewing various fabrication processes employed, its properties, microstructural analysis, applications and, finally, the future trends and challenges.

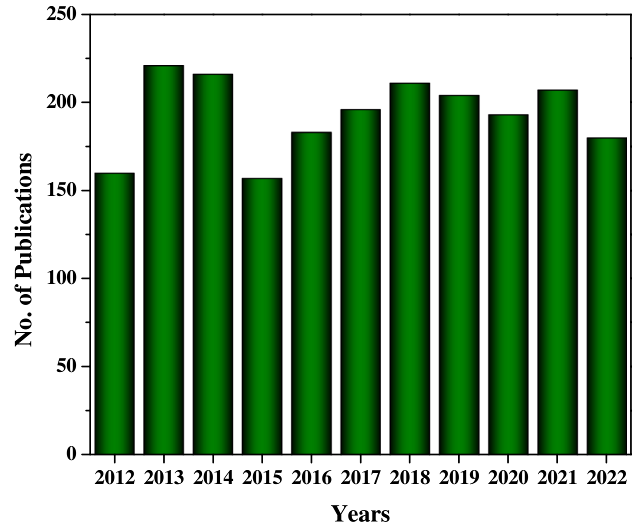

Fig. 1 Publications of ceramic coating on steel-related papers over the past 10 years (compiled from Scopus database during 01/2012–12/2022)

2 Process of Ceramic Coatings

Due to the affordability and availability of steel, the process of ceramic coatings over steel substrates has received remarkable attention. Ceramic materials have a variety of cutting-edge qualities including electrical insulation, wear resistance, corrosion resistance, and heat resistance [17, 18]. Due to their superior qualities, ceramic coatings have wide application in the industry for the past few decades as metal–ceramic combinations exhibited peculiar characteristics. In general, carbides like silicon carbide (SiC) and titanium carbide (TiC) are employed as dispersoids in the coating where hardness and wear resistance are the prime requirements. However, oxides such as titanium dioxide (TiO_2), silicon dioxide (SiO_2), and aluminium oxide/alumina (Al_2O_3) are also used as dispersoids in places where resistance to high-temperature oxidation is required in addition to improvement in hardness as well as wear [19–22]. Currently, many different ceramic coating methods are employed for various applications. The subsequent sub-sections focus on various methods like plasma electrolytic oxidation (PEO), which develops a ceramic oxide layer over the substrate without damaging the substrate due to thermal expansion, sputter deposition which aids in thin film deposition having better adhesion to the substrate. Even materials with extremely high melting points can be easily sputtered, which is a significant benefit of sputter deposition. Laser cladding which has high-speed thermal cycle helps to attain higher strength and refined microstructures, plasma spraying that can incorporate a wide variety of materials for coating and centrifugal thermite process which aid in the production of inner ceramic lining in pipelines.

2.1 Plasma Electrolytic Oxidation

Plasma Electrolytic Oxidation is a very efficient electrochemical method for treating the surface of steel. It is typically used on valve metals or their alloys, such as titanium (Ti) [23], aluminium (Al)[24], magnesium (Mg)[25], and zirconium (Zr) [26]. The component made of light metal or alloy is submerged in an electrolyte bath, depending on the desired PEO coating qualities, the bath's composition varies. The solution is passed through a high voltage current that is typically 200 V or more in voltage. A plasma discharge is produced on the substrate's surface as a result of the elevated temperatures on the alloy's surface brought by the high potentials which in turn cause the light metal substrate to primarily form crystalline oxides, such as corundum, periclase, or rutile/anatase in the case of Al, Mg, and Ti. (Fig. 2) [27]. On the surface of 10B21 steel, a ceramic coating mostly made of α-Al_2O_3 with strong resistance to corrosion and high density was effectively created [28]. Aluminate and silicate electrolytes were used to prepare PEO coatings, the oxide particle was found to be of greater size and the surface of the aluminate electrolyte coating was observed to be rough and more porous, whereas an even coating was observed for silicate electrolyte with a few large, elongated micropores [29]. γ-Al_2O_3 coating was produced on carbon steel by initially depositing an Al film followed by MAO with a current density of 45 A/dm^2, anodic voltage of 350 V, pulse frequency of ± 650 Hz, and treatment time—10 min as the parameters [30]. An oxide coating of 110 µm thickness was produced on a Q235 low-carbon steel by cathodic PEO treatment for 9 min (Fig. 3a, b). It was observed that an

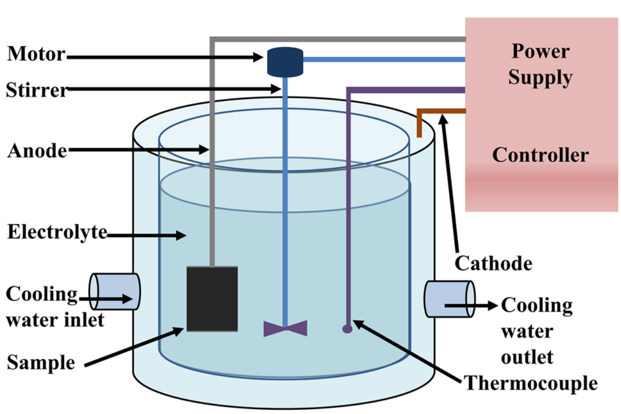

Fig. 2 Schematic illustrating the set-up used for plasma electrolytic oxidation

increase in the treatment duration had a constructive effect on thickness and surface roughness [31]. The XRD analysis indicated the presence of amorphous SiO_2 and polycrystalline Fe_2O_3 and Fe_3O_4 phases in coatings produced using sodium silicate and sodium carbonate electrolytes (Fig. 3c) [32]. Low carbon steel treated with varying wt.% of silicate resulted in a coating of composition ferric Oxide (Fe_2O_3), Fe_3O_4, and SiO_2. Dense microstructure and improved adhesion with the substrate were observed for 30 g/L silicate concentration which resulted in enhanced wear and corrosion resistance [33]. Micro-arc discharge on the material's surface was increased by adding sodium carbonate (Na_2CO_3) to the micro-arc oxidation (MAO) electrolyte which speeds up the production of Al_2O_3. The conversion of Al_2O_3 to α-Al_2O_3 is promoted, and the amount of α-Al_2O_3 in the coating was enhanced due to the synergistic action of Na_2CO_3, and sodium tetraborate ($Na_2B_4O_7$) resulted in improved surface quality (Fig. 3d) [34]. MAO with Lanthanum oxide (La_2O_3) rare earth additive was used to coat N80 steel, coatings with 1.5 g/L La_2O_3 addition exhibited higher α-Al_2O_3 content and the best wear resistance as fewer grooves were present in worn surface analysis (Fig. 3e) [35]. Composite coating of composition aluminium fluoride (AlF_3), aluminium hydroxide ($Al(OH)_3$), $Al_2Ti_7O_{15}$, α-Al_2O_3, γ-Al_2O_3, and SiO_2 were produced on S355 offshore steel via laser cladding combined with MAO (Fig. 3f). Cladding coating was composed of TiC, $AlFe_3$, $AlNi_3$, Al_2O_3, and AlFeNi and MAO area contains the elements Ni and Fe. The findings demonstrate that the cladding coating's components diffuse into the composite coating, improving their capacity to link together at the interface between the two coatings [36].

2.2 Sputter Deposition

In sputtering, atoms or molecules are expelled from the target surface as a result of ions being propelled toward a target material by a plasma. These expelled atoms subsequently go to the substrate and deposit there, resulting in the formation of a thin film. The sputter deposition is further subclassified into DC sputtering, RF sputtering, magnetron sputtering, reactive sputtering, etc. (Fig.4). SS was coated with a thin film Lithium Niobium Oxide (LNO) using RF magnetron sputtering. It was revealed that the phases indulged with the deposited LNO layer is strongly influenced by the sample's position in the plane parallel to the target plane. Without any signs of $LiNbO_3$ production, the XRD pattern of the specimen grown 50 mm from the centre of the deposition region reveals two phases of NbO and Nb_2O_5 oxides (Fig.5a). On the contrary, polycrystalline $LiNbO_3$ and $LiNb_3O_8$ are found in the centre of the deposition area (Fig. 5b) [37]. On 65G steel, a 2-µm-thick, quasi-amorphous NiB-Cr_7C_3 layer was deposited using magnetron deposition. It was discovered that the microhardness was roughly 10 GPa at an

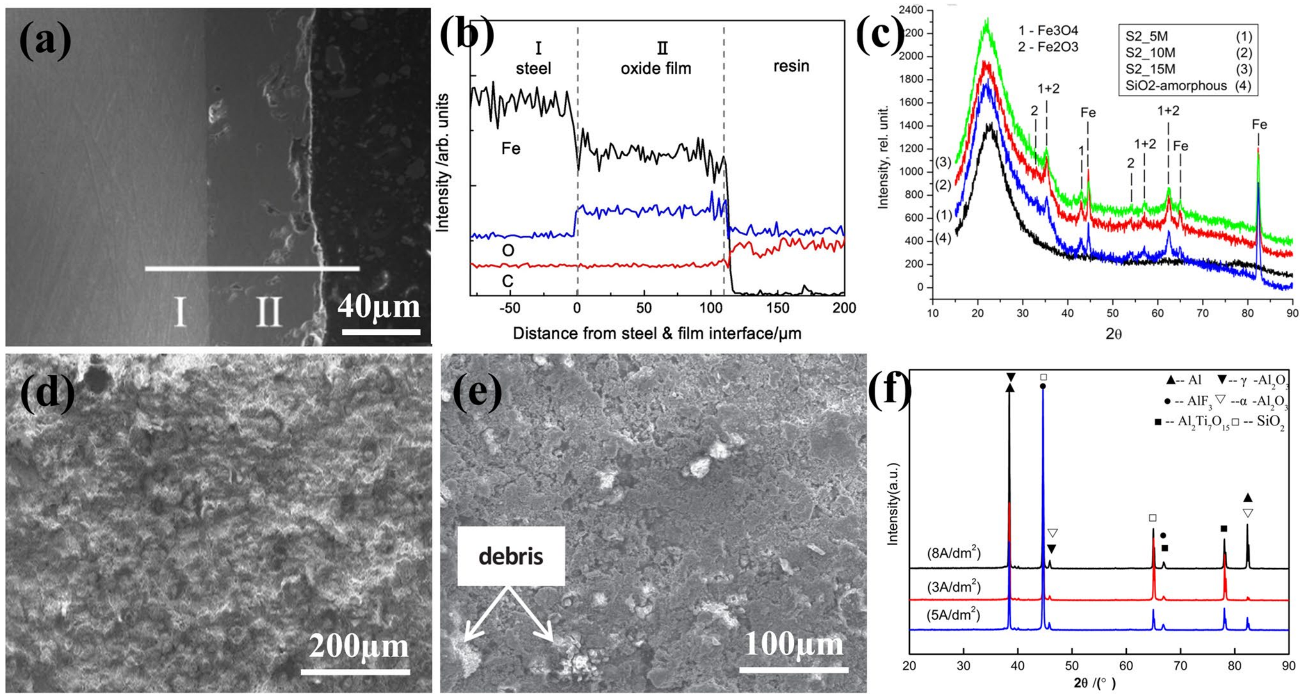

Fig. 3 (**a**) SEM image, (**b**) line scan of oxide layer cross section on Q235 steel [31], (**c**) XRD pattern of phases formed in sodium silicate and sodium carbonate electrolytes [32], (**d**) SEM image of uniform dense alumina coating produced from electrolyte composed of $NaAlO_2$, NaH_2PO_4, Na_2CO_3, and $Na_2B_4O_7$ [34], (**e**) minimal wear debris in ceramic coating with 1.5 g/L La_2O_3 [35], (f)XRD pattern of the composite coating produced via laser cladding combined with MAO [36]

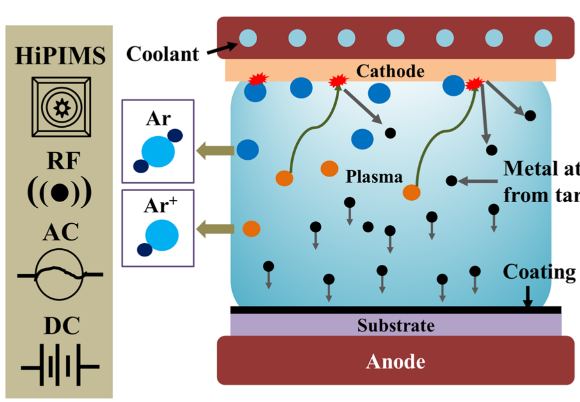

Fig. 4 Schematic illustration of sputtering deposition process

applied indentation load of 21.86 mN. Up to an increasing load of 16 N, the coating was not fully delaminating, and the failure turned out in the form of plastic deformation. When scratched, the coatings wear out but do not peel off because the wear in the coating regions is smooth and lacks distinct cleavages [38]. DC and RF magnetron sputtering was used to co-deposit (W, Be)—Cr_2O_3 and SiO_2 films on SS304 substrate. The overall hardness tends to increase with the co-deposition of Be, while it causes a negative impact with the co-deposition of W with oxides. The coefficient of friction (COF) was observed to reduce significantly in Cr_2O_3 co-deposited with W and Be having a greater reduction with Be deposition compared to that of SiO_2-deposited films [39]. Reactive magnetron sputtering was used to produce high entropy metal sublattice ceramic coatings (AlCrFeTiMo)NO and (AlCrFeTiNb)NO on a 12Cr F/M steel substrate. In comparison to the (AlCrFeTiNb)NO coating, (AlCrFeTiMo)NO coating demonstrated superior lead-bismuth eutectic (LBE) corrosion resistance with a reduced rate of oxidation corrosion. The (AlCrFeTiMo)NO coating exposed at 650°C exhibits a stable FCC structure, demonstrating the coating's structural resilience in a high-temperature LBE corrosion environment [40]. Diamond-like carbon (DLC) coating was produced on SS316L with Ti/TiC/TiN as interlayer. When methane (CH_4) was added to the deposition chamber, the deposition rate of DLC rose from 6.7 nm/min to 7.1 nm/min [41]. MgZnCa alloy coating of 4μm thickness deposited on SS304 was observed to reduce the corrosion current density by 36% compared to that of the substrate. An increment in the coating thickness to 6μm resulted in a further reduction of the corrosion current density by 47.7% compared to the uncoated sample [42]. Reactive co-sputtering was used to create (AlCrNbSiTiV-W)N films on SS304 substrates with variable $N_2/(Ar+N_2)$ flow ratios. The coating's mechanical, tribological, and corrosion characteristics improved when the flow ratio of $N_2/(Ar+N_2)$ reached 20% [43]. CrN/CrAlN multilayer ceramic coating was deposited on

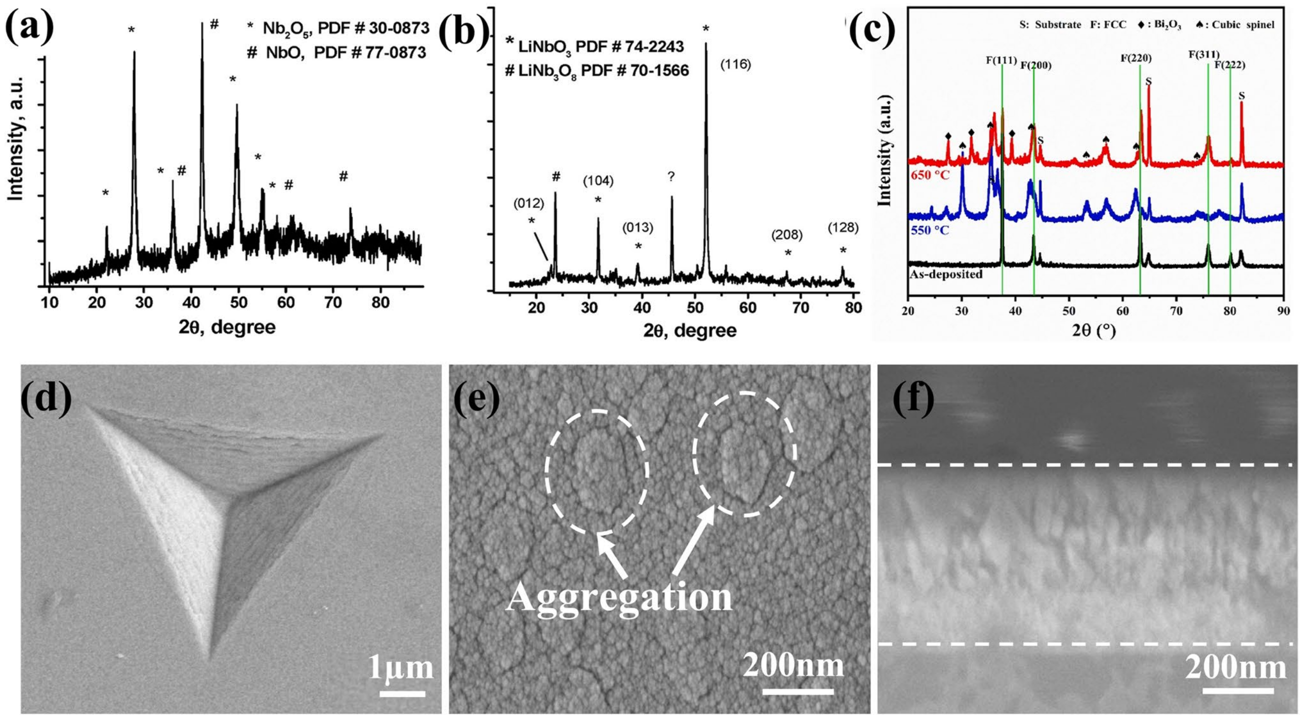

Fig. 5 XRD diffraction pattern of (**a**) LNO layer at 50 mm from centre, (**b**) at centre [37], (**c**) (AlCrFeTiMo)NO coating LBE exposed at 550 °C and 650 °C [40], SEM image of (**d**) cube corner imprint of TiC/TaC superlattice [45], SEM images of (ZrNbMo-Al-N) film after annealing at 700 °C (**e**) surface, and (**f**) cross section [46]

AISI440 martensitic steel via high-power impulse (HiPIMS) and DC magnetron sputtering process. The coating with Cr as the base layer exhibited lower residual stress due to the stress-relieving effect caused by Cr and improved resistance to plastic deformation due to the harder CrAlN outer layer enriched by the HiPIMS process [44]. Superlattice films of TaC/HfC and TiC/TaC were developed on austenitic SS via non-reactive and pulsed DC magnetron sputtering. TiC/TaC superlattice was observed to have improved microhardness and fracture properties compared to TaC/HfC and constituent monolithic films as the cube corner imprint of TiC/TaC subjected to 450mN was devoid of any radial cracks (Fig.5d) [45]. Tri-layer (ZrNbMo–Al–N) films were deposited on SS using reactive magnetron co-sputtering. The absorbers on SS substrates exhibit greater thermal robustness after being annealed at 400 °C for 168 hrs in a vacuum environment. Because of grain aggregations and gaps between the columnar particles, annealing at 700 °C was found to significantly reduce optical performance (Fig.5e, f) [46].

2.3 Laser Cladding

Laser deposition-related ceramic coating techniques, including laser cladding and laser remelting, are used due to their versatility, coating efficiency, time savings, and high energy density (Fig. 6). Additionally, the surface coating's

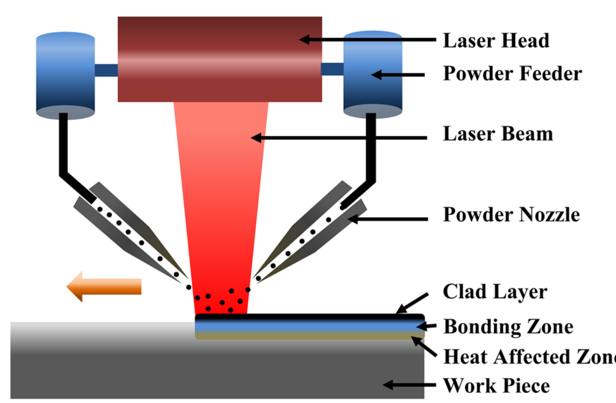

Fig. 6 Schematic illustration of laser cladding process

homogeneous, fine microstructure and strong bond that exists between the substrate and coating, rapid heating and cooling rates, make them more noticeable. TiC coating was produced on Ti6Al4V substrate, the ceramic coating was created by laser cladding with pre-placed nanoparticle TiC powder, and the ideal process parameters were laser power (300 W), scanning speed (5 mm/s), powder thickness (0.4 mm), and overlapping ratio (20%) [47]. Composite of H13 steel matrix reinforced with coarse TiC particles was produced by laser cladding. The produced composite layer had the highest hardness of 1365 HV, which was about twice that of the base substrate. An austenitic structure, in addition to the TiC phase and martensite, was found when the volume of TiC was increased by more than 60% (Fig. 7f) [48]. An improvement in the wear resistance of 316L steel was observed by TiC, Niobium carbide (NbC) ceramic-reinforced composite coatings. The wear mechanism was observed to transform from intense adhesive wear along with plastic deformation to a minimum delamination mode of adhesive and abrasive wear [49]. Ti and Boron carbide (B_4C) mixed powders were used to create in-situ laser-clad TiC/TiB composite bioinert ceramic coatings. As the heat treatment temperature increased, the residual tensile stress in the heat-treated coatings dropped. Average residual stress values for heat-treated coatings at 400 °C, 600 °C, and 800 °C were 0.96, 0.66, and 0.48 GPa, respectively, compared to 1.53 GPa for untreated coatings [50]. Fe-based fluxing powder with the addition of Ti, TiN, C were mixed with different wt.% of Cerium dioxide (CeO_2) and laser cladded on a steel plate, the coating's penetrating cracks are successfully weakened by the addition of CeO_2, which also lessens the sensitivity of cracks and porosities. The coating with 2.5 wt.% CeO_2 inclusion exhibits the maximum microhardness value of 709.46 HV, which is mostly brought on by fine grain strengthening and boosting the development of the hard phase [51]. Ceramic coating of Al_2O_3–Titanium diboride (TiB_2)–TiC was fabricated over carbon steel with varying concentrations of Al_2O_3. The coating with 30% concentration depicted superior quality while the increased concentration of Al_2O_3 resulted in the less dense coating due to reduced wettability between TiB_2 and Al_2O_3 during solidification [52]. A Synergistic effect of precipitation hardening, and microstructural refinement achieved by coating TiC on AISI 410 martensitic SS provided improved microhardness and wear resistance [53]. The inclusion of B_4C in the composite ceramic coating of Ni_20_4 improved the wear resistance due to fine grain strengthening, solid solution strengthening, and dispersion strengthening. The worn surface was smoother and had shallow wear marks (Fig. 7e) [54]. Ni–Tungsten carbide (WC)–calcium fluoride (CaF_2) coating was produced on medium carbon steel via laser cladding assisted with ultrasonic vibration processing and the cross-section analysis revealed that the coating produced is devoid of crack or porosity (Fig. 7a) [55]. The addition of La_2O_3 in Ni-based ceramic coating resulted in producing a crack-free coating combined with microstructural refinement (Fig. 7b) which improved the corrosion resistance and microhardness [56]. The increased microhardness of the Al_2O_3–Ni composite coating was due to the hard phases formed as Ni combined with Fe, Al, and Cr as inferred from the cross-sectional XRD (Fig. 7c) [57]. Analysis of wear mechanism of the Vanadium carbide (VC)- Chromium carbide (Cr_7C_3) coating proved the wear mechanism to be a mixed adhesive and micro-polishing type (Fig. 7d) [58].

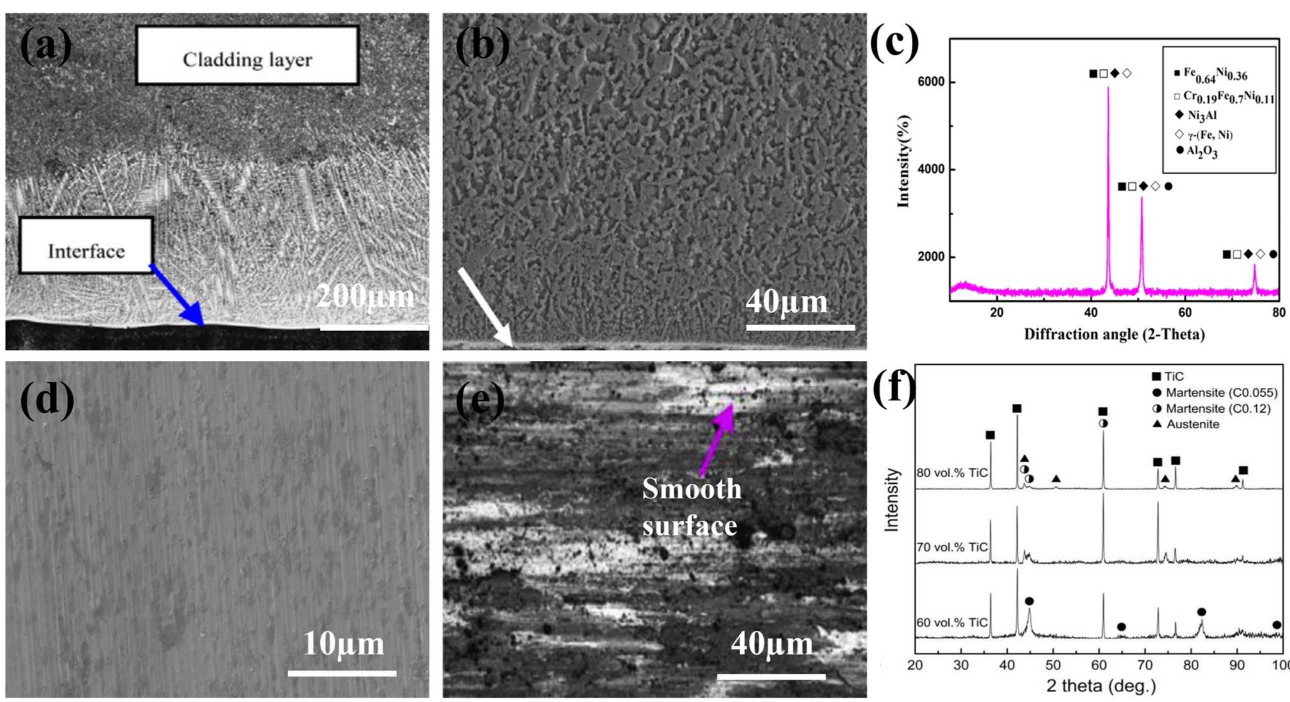

Fig. 7 SEM micrographs of (**a**)laser cladded dense Ni–WC–CaF_2 [55], (**b**) dense microstructure with La_2O_3 inclusion [56], (**c**) XRD pattern of hard phases formed in Al_2O_3–Ni Coating [57], (**d**) worn surface of VC-Cr_7C_3 coating [58], (**e**) worn surface of coating with 10 wt% TiC, TiN, and B_4C [54], (**f**) XRD pattern indicating the phases formed in TiC/H13 deposit with 60% volume fraction of TiC [48]

2.4 Plasma Spraying

Spraying technique that is frequently employed in ceramic coating is plasma spraying. The direct current plasma arc sprays and deposits coating ingredients on the substrate (Fig. 8). Plasma spraying technique was used to coat carbon steel with Al_2O_3-40 wt.% TiO_2, which reduced the splat delamination and wear rate compared to the uncoated samples [59]. Al_2O_3-40 wt.% TiO_2 was coated on AISI 1045 steel roller, and the influence of rolling stress was investigated, spalling, surface abrasion, and delamination were the modes of failure observed. The mechanism of delamination was observed to be a combination of interfacial cracks and fatigue micro-cracks from micro-defects within the coating (Fig. 9d) [60]. Plasma-sprayed Al_2O_3 coating on austenitic SS was laser processed with varying parameters and θ-Al_2O_3 was observed in the laser-remelted samples (Fig. 9e). The sample was remelted with 600W power, and 5 mm/s laser velocity showed improved fracture toughness and tribological properties as compared to the as-sprayed samples [61]. The various benefits of the low-pressure plasma-sprayed thin-film coating technique and chances to alter the features of the coating as well as its consequent microstructure were studied. Vapour depositions tend to produce columnar coatings, whereas dense coatings were produced by droplet deposition. The size of the plasma plume was increased by low operating pressure which resulted in homogenous coatings [62]. Steel substrate was coated with WC-12% cobalt (Co) with two types of particle size and morphology. The powder size of 45 μm and spherical morphology resulted in a dense structure and less porosity providing increased microhardness. The effect of heat treatment was analysed at 500, 900, and 1100 °C and the coated sample heat treated at 500 °C

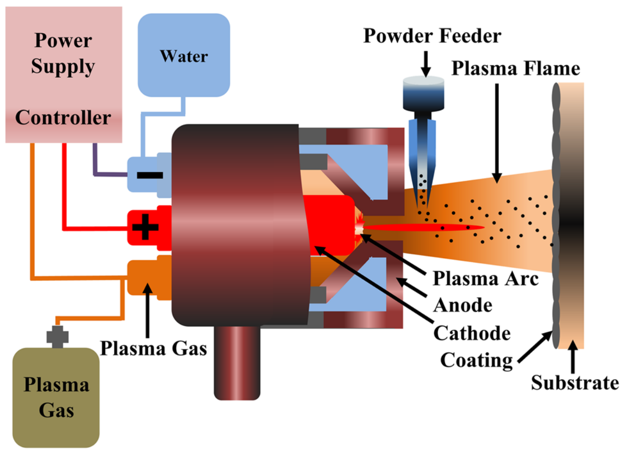

Fig. 8 Experimental set-up used for Plasma Spraying Process

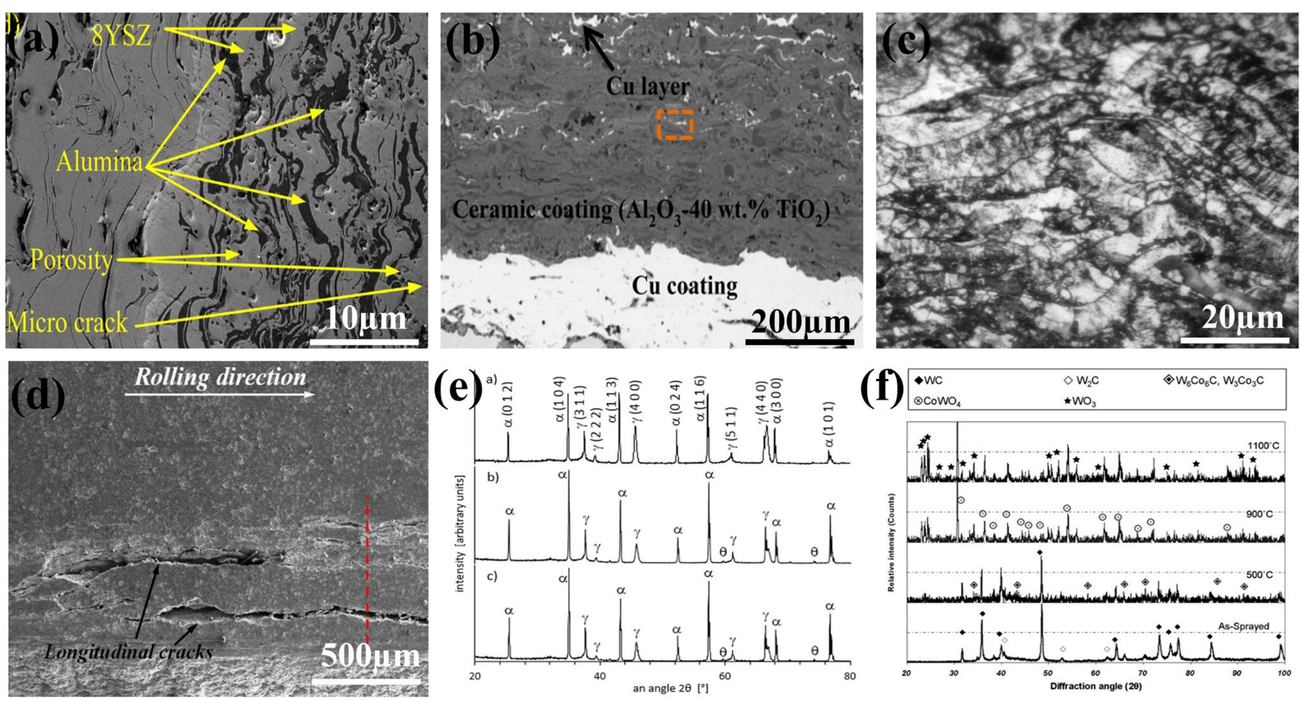

Fig. 9 SEM image of (**a**) homogeneous distribution of alumina in composite coating [66], (**b**)cross-sectional view of composite coating with Cu layer [67], (**c**) diamond-reinforced composite coating [68], (**d**) Surface morphology of longitudinal cracks in Al_2O_3-40 wt.% TiO_2 coating on AISI 1045 steel [60], (**e**) XRD analysis: a) the as-sprayed coated; **b**) laser re-melted LP coated, and **c**) laser re-melted HP coated [61], (**f**) XRD pattern of atmospheric plasma-sprayed (APS) WC–Co coating, before and after heat treatment in atmosphere [63]

exhibited improved microhardness due to the formation of η-carbides (Fig. 9f) [63]. AISI 304 steel was coated with 60 wt.% NiCrSiB-40 wt.% Al_2O_3 with an average density of 6 g/cm^3, surface roughness 8.5 µm, and adhesion strength 18.2–22.4 MPa [64]. SS304 was coated with chromium (III) oxide (Cr_2O_3)–Al_2O_3 which was then sealed by Aluminium Phosphate ($AlPO_4$) with little amount of Al_2O_3 nanoparticles. The subsequent heat treatment at 600 °C for 30 min was carried out and was tested for the corrosion. It was noted that the sealant effectively resists corrosion [65]. Addition of 3 wt.% Carbon nanotubes (CNT) to alumina feedstock powder resulted in a coating with increased homogeneity in alumina dispersion (Fig. 9a) as CNT have higher heat capacity which maintains alumina in molten state for longer periods [66]. As the voids in the ceramic layer act as fracture sources due to stress concentration, adding a copper (Cu) metal barrier layer (Fig. 9b) to an Al_2O_3-40 wt.% TiO_2 ceramic coating improved the anti-crack propagation ability. The Cu layer also assisted with crack deflection, bridging, and particle pull-out. [67]. Successful retention of diamond was observed in bearing steel coated with diamond reinforced molybdenum feedstock (Fig. 9c) with a minute graphite content present in the coating due to the partial degradation of diamond because of exposure to high-temperature arc [68]. Mild carbon steel was coated with Titanium Carbo-Nitride (TiCN) and the effect of spray distance on mechanical properties were evaluated. Due to the particles' complete melting and homogeneous spread-out, which resulted in a closely bonded structure, the maximum hardness, elastic modulus, and bonding strength were seen for a spray distance of 100 mm [69]. Micropores were observed in AISI 1020 steel coated with $Al_2O_3 + TiO_2$, CNT were added to the feed stock and subsequently micropores and the percentage of porosity were reduced as the fraction of CNT is increased. This results from the surface reaction and metallurgical fusion of CNT with Al_2O_3 and TiO_2, which in turn increase the surface hardness [70]. The properties and additional characteristics of the coatings fabricated via various processes are given in Table 1.

There are several methods to produce ceramic coatings on steel and the choice of method relies on the specific requirements of the application, including the desired properties of the coating and the behaviour of the substrate. Among these methods, thermal spray and plasma spraying are generally considered the best method to produce oxide ceramic coatings on steel compared to chemical vapour deposition (CVD), sol–gel, anodizing, etc., due to their ability to produce dense and uniform coatings with high bond strength and corrosion resistance [71]. The inter-lamellar bonding of the ceramic coating can be improved by raising the deposition temperature of the coating. When an oxide ceramic coating is being deposited at a temperature greater than the critical bonding temperature, the bonding ratio of the coating considerably rises, improving the coating's adhesive strength [72]. The intersplat bonding quality, which predominates in the mechanical properties, determines the cohesive strength of ceramic coatings. Higher particle velocities result in stronger cohesion, which may be explained by a high interface bonding ratio. Higher dynamic pressure results in closer contact between the spreading spray particles and the splats below due to higher particle velocity impact [73]. Carbon steel (C45) was coated with Al_2O_3–TiO_2 utilizing the high-velocity oxy-fuel (HVOF) and plasma spraying. In contrast to HVOF coating technique, high temperature generated in the plasma coating method resulted in the melting of ceramic powders and the development of totally melted patches on the coated surfaces [74]. The production of carbide coatings over steel substrates can be achieved via thermal spraying, physical vapour deposition (PVD), CVD, electroplating, etc. When the current-to-flow volume ratio is high and the ratio of secondary hydrogen flow to the total flow is also high, carbide coatings exhibit better powder deposition, fewer porosities, and more molten particles [75]. The formation of an oxide layer during the spraying process is a critical factor, as the thickness, stability, and mechanical strength of the oxide layer protect the underlying surface from degradation [76]. The spraying process caused the oxide phases to change from crystalline to amorphous condition. The high particle-in-flight velocities cause the splats to spread out and expand, creating lamellae with vast surface areas. This makes it possible for the subsequent rapid solidification to occur quickly enough to create an amorphous phase [77]. Due to the high temperature generated while deposition, the transition of Cr_3C_2 from feed stock into Cr_7C_3 and $Cr_{23}C_6$ crystalline phases was observed in SS410 APS coated with Cr_3C_2-25NiCr [78]. Dense and uniform nitride coatings with high hardness and wear resistance can be produced on steel via PVD and CVD. At elevated temperature conditions, multilayer coatings of nitride with nanoscale bilayer thickness exhibit exceptional hardness and increased resistance to wear. The creation of a protective surface oxide and the multilayer structure work together to prevent cracks from spreading, and additional oxidation increases wear resistance [79]. With a 25% N_2 gas flow ratio, the Mo–Si–N coating produced by DC magnetron sputtering demonstrated exceptional mechanical properties. The fabrication of the Mo–Si–N coatings involved managing chamber pressures between 1 and 10 mTorr at a 25% N_2 gas flow ratio at room temperature in order to increase coating's density and decrease the likelihood of contamination while preserving an amorphous structure. An increase in coating density, hardness, and elastic modulus, as well as a drop in O content, were caused by a reduced working pressure of 1–2.5mTorr [80]. Very hard and self-lubricating TiSiCN coatings were produced on H13 steel using plasma-enhanced CVD, and they had a nanocomposite structure made of an

Table 1 Comprehensive evaluation of ceramic coatings produced—process and properties

Process	Substrate	Coating/phases	Process parameters	Pre/post-treatments	Thickness of coating	Mechanical Properties	Wear/Corrosion properties	Ref.
PEO	AerMet100	$FeAl_2O_4$, Al_2O_3	Current density—5 A/dm^2 Frequency—400 Hz Duty cycle—4% Treatment time—20 min	Hot dip aluminium plating	25 µm	–	Corrosion potential, E_{corr}(− 0.7063 V), Wear—2.58 × 10^{-7} mm^3/Nmm	[82]
	AISI 316L	Fe_3O_4, Al_2O_3	Voltage—320 V Treatment times—3 min	Autoclaving	–	–	Corrosion—E_{corr}(-212.148 mV)	[83]
	Q235 carbon steel	Fe_3O_4, $FeAl_2O_4$	Voltage—100 V Pulse frequency—2000 Hz Treatment time—10–50 min	–	–	Tensile strength—20.6 MPa Shearing strength—16 MPa Thermal shock resistance—9 cycles at 300^{0}C	–	[84]
	AISI 316L steel	FeO_x, Al_2O_3	Voltage—320 V, Treatment time—10 min, aqueous electrolyte—0.1 M $NaAlO_2$ + 0.05 M NaOH, electrolyte < 45 °C	Autoclaving	30 µm	–	Corrosion—E_{corr} (− 0.3 V, –0.245 V)	[85]
	Galvalume coated carbon steel	Al_2O_3, Al_2SiO_5, $NaAlSiO_4$	Direct Current (DC) mode: Current density 0.5 A/cm^2, treatment time 90 s Unipolar Pulsed Current mode (UPC): 1 A/cm^2, treatment time 120 s	–	20 µm	–	Corrosion—E_{corr} (− 1.19 V), corrosion current density, I_{corr} (2.28 × 10^{-6} A/cm^2)	[86]

Table 1 (continued)

Process	Substrate	Coating/phases	Process parameters	Pre/post-treatments	Thickness of coating	Mechanical Properties	Wear/Corrosion properties	Ref.
Plasma Spraying	IN-625, Rolled Alloys	$La_2Zr_2O_7$	Voltage—69 V Current—300A Spray distance—90 mm	–	250 µm	–	Hot corrosion (1000 °C, V_2O_5)	[87]
	SS	NiCrAlY, Slurry spray—Al_2O_3	Plasma spray Voltage—65 V Current—450A Spraying distance—150 mm Slurry spray Atmospheric pressure—1.2 MPa Spraying angle—45° Spraying distance—300 mm	Slurry spraying	100 µm	Thermal shock resistance—14 cycles at 800^{0}C	–	[88]
	Carbon steel	TiB_2 TiC, TiO_2, Ti-B_4C	Voltage—70 V Current—500A Spraying distance—100 mm	–	300 µm	Porosity—(TiB2–TiC)—27.5%, (Ti-B_4C)—10.8% Microhardness-(TiB_2–TiC)—681$HV_{0.1}$, (Ti-B_4C)—1241 $HV_{0.1}$	–	[89]
	1Cr18Ni9Ti SS	α-Al2O3 γ-Al2O3	Voltage—60 V Current—550A Spraying distance—90 mm	–	350 µm	Bonding strength—25.4 MPa Microhardness—1061HV	–	[90]
	SS304l	Ni–Al (bond coat) Cr_2O_3-YSZ (top layer)	Voltage—57 V Current- 600A Spraying distance—110 mm (bond coat) Spraying distance—60 mm (top layer)	Sealed the top layer with bisphenol A and heated at 120 °C for 15 min	Mean thickness—280 ± 15 µm	Porosity—10.2 ± 2.7% icrohardness—799HV Fracture toughness—108.0 ± 1.5 MPa $m^{1/2}$	COF—(0.11–0.15) Mass loss—11 mg Wear rate—207×10^{-6} mm^3/Nm Corrosion—E_{corr} (–0.220 V) I_{corr} (0.03 µA/cm^2)	[91]

Table 1 (continued)

Process	Substrate	Coating/phases	Process parameters	Pre/post-treatments	Thickness of coating	Mechanical Properties	Wear/Corrosion properties	Ref.
Laser cladding	5CrNiMo die steel	α-Fe, $(Ti,Mo)B_2$, (Ti, Mo)C and $(Fe,Cr)_7C_3$	Laser power—800 W Scan speed—5 mm/s Beam diameter—2 mm Overlap rate—30%	Quenching and tempering	1 mm	Oxidation resistance– 600 °C		[92]
	Q550 high strength low alloy steel	Cr_3Ni_2, Cr_3C_2, $(Cr, W)_{23}C_6$, W_2C, NiCx, Cr_5B_3, and W_2B_5	Laser power -3.6 kW Laser scan speed—3 mm/s Rectangle laser spot—17 mm × 1.5 mm	Dried at 250 °C for 30 min	1 mm	–	Wear resistance (weight loss—14 mg)	[93]
	AISI 410 martensitic SS	$Cr_{23}C_6$, $Fe_{23}C_6$, TiC	Laser power—480 W Spot diameter—1.2 mm Traverse speed—480 mm/min Energy density—100 J/mm^3 Overlap rate—50% Powder delivery rate—6.5 g/min	–	1 mm	Microhardness—735HV	Wear rate—0.149×10^{-5} mm^3	[53]
	SS304	ZrB_2 TiB_2 (Zr_x, Ti_{1-x}) B_2	Laser power—2.5 K W Scan speed—100 mm/s Powder delivery rate—7.2 g/min Overlap rate—80%	–	–	Microhardness—$1130HV_{0.5}$	Wear rate—5×10^{-6} mm^3/Nm	[94]
	AISI420 martensitic SS	VC V_8C_7	Laser power—3.2 K W Scan speed—5 mm/s Powder delivery rate—0.618 g/s Overlap rate—25%	Substrate preheated at 250 °C	–	Microhardness—(626.5—681.1 HV)—10% VC (790–840 HV) 40% VC	Erosion resistance increased by 9.15% (10% VC), 46.75% (40% VC) Corrosion—E_{corr} (– 0.349 V, 10%VC), (– 0.521 V–40% VC) I_{corr} (0.349 μA/cm^2—10%VC), (0.619 **μ**A /cm^2—40%VC)	[95]

Table 1 (continued)

Process	Substrate	Coating/phases	Process parameters	Pre/post-treatments	Thickness of coating	Mechanical Properties	Wear/Corrosion properties	Ref.
Sputter Deposition	AISI440	CrN, CrAlN	Sputtering power—900W, frequency 500 Hz Chamber pressure—2.67×10^{-1} Pa Atmosphere—Ar	–	11.3 µm	Hardness—21 ± 3 GPa	Wear depth—4 µm (approx)	[44]
	SS304	(AlCrNbSiTiV-W)N	Sputtering power—200W Substrate temperature—150 °C	–		Hardness—37.52 GPa, Young's modulus—210.4 GPa	COF—0.516, Corrosion—E_{corr} (–0.07 mV)	[43]
	SS304	MgZnCa	Sputtering power-80W Deposition rate—9 nm/min Working pressure—0.5 Pa	–	6 µm	–	Corrosion—E_{corr} (–0.07 V) I_{corr} (0.26 mA/cm^2)	[42]
	SS316L	TiC	Sputtering power—150W Substrate temperature—250 °C Chamber pressure—2×10^{-3} mbar Atmosphere—Ar	Target pre sputtered for 5 min	2.1 µm	–	Corrosion—E_{corr} (–0.219 V) I_{corr} (0.121 µA/cm^2) Corrosion inhibition efficiency—98%	[96]

amorphous SiCN matrix that contains TiCN nanocrystals. Coating adhesion improves significantly in the presence of the graded interlayer (Ti/TiN/TiCN) exhibiting improved mechanical properties [81]. Overall evaluation of coating deposited over steel reveals that thermal spray processing best suits to produce oxide and carbide coating while PVD and CVD can be employed for the production of nitride coatings to best suit the desired applications.

2.5 Self-Propagating High-Temperature Synthesis—Centrifugal Thermite Process

The processes discussed so far hold good for developing a ceramic coating over outer surfaces. However, pipelines used for the transport of slurry, reactive materials, chemicals, etc., also undergo extensive abrasion, erosion, and corrosion. Thus, it is very much required to coat the inner surface of the pipelines, thereby reducing its maintenance and downtime. The centrifugal thermite process involves producing a ceramic lining inside a hollow cylinder/pipe by virtue of thermite reaction or self-propagating high-temperature synthesis (SHS) where the reactant mixtures are loaded in the tube and rotated at high speed and then the mixture will be ignited using a heated tungsten filament or by burning magnesium ribbon once the required velocity is reached. The reaction increases the temperature due to its exothermic nature and propagates throughout, the density difference between the formed products results in forming an inner ceramic lining and an intermediate intermetallic layer (Fig. 10) [97]. The production of cast granules with particle sizes ranging from 0.2 to 4.0 mm was accomplished using thin-layer SHS reactions of the thermite type made of Nickel oxide (NiO) and Aluminium (Al) powders at atmospheric pressure. Variations in the layer thickness of the mixture employed and the amount of neutral diluent (αAl_2O_3) used had an impact on the structure and size of SHS-generated granules [98]. Dendritic-structured Al_2O_3 was observed as the dominant phase due to the rapid heat dissipation from the outer

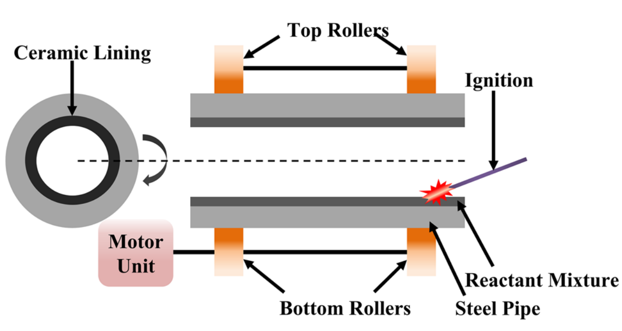

Fig. 10 Schematic illustrating the experimental set-up of centrifugal thermite process

pipe surface and Al_2O_3 was surrounded by spinal-shaped hercynite ($FeAl_2O_4$) due to the higher melting point of Al_2O_3, which resulted in nucleation and growth of alumina followed by the solidification of $FeAl_2O_4$ [99]. Abrasion test conducted on the ceramic lined pipe with SiO_2 slurry flowing at 2.5 m/s for 900 h revealed that the wear loss of ceramic lined pipe was lower than 10% of SS41 and 12.5% of S45C steel pipes [100].

The inclusion of Al_2O_3 in the thermite mixture and the use of tungsten filament for ignition instead of oxyacetylene flame reduced the risks of violent reaction, splashing of molten particles and fumes evolved [101]. The addition of 4 wt.% SiO_2 in the reactant mixture improved the density to 3.69 g cm^{-3} and reduced the porosity to 3.1% of the ceramic lining. It also increased the microhardness to 1566HV$_1$ and fracture toughness values to 4.125 MPa m$^{1/2}$, exhibiting lowest crack length (Fig. 11f) [102]. Al_2O_3 and Zirconium dioxide (ZrO_2) were crystallized as leading phases in hypoeutectic and hypereutectic multiphase melt, respectively, as observed in $Al_2O_3 + ZrO_2$ multiphase ceramic-lined composite pipes [103]. The microstructural analysis of the fractured specimens indicated that the fracture was not initiated at the interface of substrate and transition layer due to the strong metallurgical bonding as observed in Al_2O_3–TiO_2–TiC multiphase ceramic layer with AlFe–AlCrFe–NiFe intermetallic layer (Fig. 11e) [104]. The addition of Cerium oxide (CeO_2) and glass powders to the thermite mixture resulted in the production of $FeAl_2O_4$ free ceramic lining that aid in the application in corrosive environment [105]. Effect of centrifugal force was analysed for Ti–B–C system, producing TiB_2 and TiC via combustion synthesis. It was revealed that the faster reaction propagation occurs under inverse centrifugal direction [106]. It was discovered that preheating the carbon steel pipe prior to the process lengthens the period that molten products would remain in a liquid form. Additionally, increasing the molten products' fluidity by adding Calcium fluoride (CaF_2) to the thermite can assist in reducing inclusions. CaF_2 had further desulphurizing and dephosphorizing effects. The inclusions in the SS were greatly decreased once the method was improved [107]. Pre-coating of the substrate with NiCrAl and NiO + Al showed improvement in thermal shock resistance and nickel oxide (NiO) + Al precoat had improved bonding with the surface having Ni and Fe diffused across the interface (Fig. 11b, c) [108]. Under the influence of the centrifugal acceleration field, a functionally graded coating was generated. The Al_2O_3, Fe, and byproducts of the thermite process, entered the TiC pellet to form a robust intermetallic layer. The XRD pattern revealed tetragonal titanium aluminide (TiAl, Ti_3Al) intermetallic in the compound (Fig. 11d). Intermetallic compounds that are present improve crystal characteristics by creating ordered crystal formations [109]. The ideal combination of hardness, crushing strength, fracture toughness, and mechanical

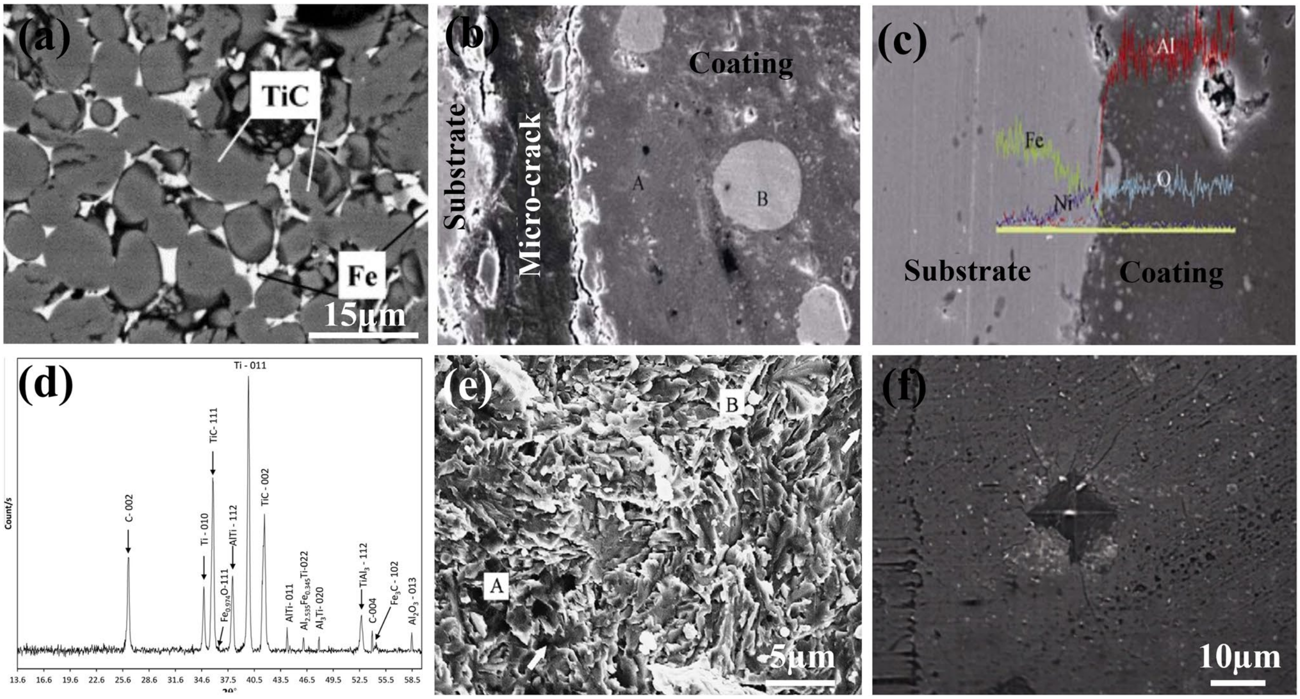

Fig. 11 (**a**)SEM image showing spherical TiC binded by Fe in TiC–xFe combustion synthesis [116], cross-sectional SEM image of (**b**) substrate and coating without transition layer, (**c**) coated sample with transition layer [108], (**d**) XRD pattern indicating the presence of TiAl, Ti_3Al intermetallic in TiC, Al_2O_3, Fe ceramic coating [109], (**e**) Fracture image of Al_2O_3–TiO_2–TiC multiphase ceramic layer with crack-free intermetallic region [104], (**f**) SEM image indicating indentation cracks on 4 wt.% SiO_2-added ceramic coating [102]

shock resistance was produced by adding 4–6% ZrO_2 to an Al–Fe_2O_3 thermite mixture [110].

Zirconia-toughened alumina ceramic lining was found to have Al_2O_3, $FeAl_2O_4$, and t-ZrO_2 phases, the t-ZrO_2 phase was accountable for improved fracture toughness [111]. Replacement of Al partially by silicon sludge with a composition of 30% Si and 70% SiC in thermite mixture increased the ceramic layer density to 3.5 g/cm^3 due to the formation of mullite ($Al_6Si_2O_{13}$), maximum hardness of the ceramic layer was found to be 1780HV. Using 10% silicon sludge, a dense ceramic layer with α -Al_2O_3 grains in dendritic structure surrounded by $FeAl_2O_4$ was formed (Fig. 11f) [112]. It was discovered that the mechanism of molten Fe deposition and penetration into TiC was majorly dependent on temperature, density as well as time profile in the reactions Fe_2O_3 + Al and Ti + C under centrifugal force. [113]. Crack pinning by fine TiB_2 platelets and crack bridging by (Ti,W)C grains were the toughening mechanisms responsible for superior fracture toughness and hardness as observed in TiB_2–(Ti,W)C ceramics [114]. An increment in centrifugal force to 200G resulted in an improvement in density to 98.6% as observed in Al_2O_3/YSZ composite ceramic lining with a composition of α-Al_2O_3, t-ZrO_2, m-ZrO_2, and Cr [115]. Combustion synthesis of TiC–xFe revealed that the increase the Fe content resulted in a drop in the combustion temperature and wave velocity. The microstructural analysis revealed that the carbide grains were of spherical in shape surrounded by Fe as a binder (Fig. 11a). The addition of 60 wt.% Fe was found to be the limit as more than that self-propagating nature of the reaction was lost [116]. Calcium peroxide (CaO_2) and Al additives in Fe–WB ceramic lining reduced the porosity and improved toughness and adhesion between coating and substrate [117]. N80 steel pipe coated with Al_2O_3 exhibited a fracture strength of 269 MPa and improved wear resistance with a reduced volumetric loss of $3.6 \times 10^{-13} m^3\ m^{-1}$ [118]. It was discovered that addition of Cr_2O_3 increased abrasion resistance, SiO_2 addition reduced the lining's surface roughness, and graphite addition boosted the lining's strength and reduced separation from steel walls [119]. Fe_2O_3 and Al powders were mixed to obtain a coating of Al_2O_3 on a carbon steel pipe of which the characterization revealed the ceramic layer primarily had α-Al_2O_3 and $FeAl_2O_4$ and the grain size expands to the inner part where thermite mixture is high. The hardness and density of the produced ceramic layer were 1430HV and 2.9 g/cm^3 without SiO_2 additive, whereas 1700HV and 3.7 g/cm^3 with SiO_2 additive [120]. When TiC–TiB_2 ceramics solidified, the TiC spherical grain matrix showed the leading growth in hypoeutectic composite, whereas the TiB_2 platelets with small aspect ratio showed the leading growth in the hypereutectic composite [121]. The use of high gravity field of 200 g centrifugal force aided in the production of 99% dense

TiB_2–TiC composite [122]. The circumferential thermal stress and interfacial stress values increased with an increase in the thickness of the SHS layer. The circumferential thermal stress in the ceramic coating increased by 84.28 MPa as thickness increased from 3.5 to 4 mm [123]. Table 2 provides the SHS-CT process ceramic coating evaluation.

3 Applications

Surface coatings are widely employed in the fields of electronics, food, mining, aviation, and transportation as well as in the chemical and petroleum sectors. In several specialist fields, surface coatings have recently seen an increase in use, such uses include thermal-sprayed coatings in sports sector, automotive, aerospace, marine, petroleum, mining, and power production industries (Fig. 12). Surface coatings offer a variety of options for changing the component qualities. Common coatings include oxides, nitrides, carbides, DLC, decorative coatings, and thermal barrier coatings. Without covering the tools with a thin layer of ceramic, it is impossible to complete modern cutting applications. Some applications include cutting non-ferrous abrasive materials at high speeds and machining extremely hard materials like Ti and AlSi alloy. Typically, the coatings used on tool surfaces are several microns thick. They lessen friction and minimize diffusion, improving cutting-edge wear resistance [125]. Erosion–corrosion issues frequently degrade boiler walls in power stations and other utility components of coal-fired industries affecting the dependability and economics of these systems. High temperatures and hostile atmospheres are characteristics of the environment within the furnaces, which cause corrosive deposits to adhere to the walls and get eroded due to ash particles [126]. Composite coatings based on Al-SiC were found to be applicable in the automotive industry that have better wear resistance [127].

In a coal-fired boiler environment, Cr_3C_2–NiCr ceramic coatings resulted in enhancing erosion as well as corrosion resistance [128]. NiTi alloy coating was found to reduce erosive wear in aerospace applications in compressor blades of aircraft [129]. CrN coating over SS304 was found to possess superior corrosion resistance and is hence suitable for marine applications [130]. Al_2O_3–13TiO_2 coatings were fabricated over C45 steel pipe that was proven to have significant applications in the petroleum industry [74]. Yttria-stabilized zirconia coating was found to have significant use in high-temperature applications by virtue of its porous microstructure which reduce thermal conductivity [131]. Cr_3C_2-20NiCr and Al_2O_3-40%TiO_2 coatings were found to increase the life span of oil piping and related devices in the oil and gas industry [132]. Ceramic coating had been used to protect the tube material such as carbon and CrMo steels from corrosion in the biomass energy industry [133]. WC–(W,Cr)$_2$C–Ni coating on SS was found to provide better resistance in high-temperature wear conditions having potential applications in aerospace and automotive industries [134]. Preoxidized SS was coated with $(Co,Mn)_3O_4$ which was used as interconnects in solid oxide fuel cell [135]. Cast iron coated with Al_2O_3, Cr_2O_3, ZrO_2 was analysed for various properties and ZrO_2 coating was found to have improved thermal shock resistance, having potential application in piston rings, cylinder liners, piston crown surface, cylinder cover, and valve parts as in automotive industry [136]. The combination of surface mechanical attrition treatment (SMAT) and low-temperature annealing at 400 $^{\circ}$C resulted in greater resistance to corrosion for SS316. The annealing process relieved residual stress and freed trapped high strain energy, facilitating the creation of nucleation sites. This enabled Cr to migrate to the surface of the material more easily and form a thick oxide layer, resulting in a reduced corrosion rate at the surface having potential application in manufacturing and automotive industries [137]. Al_2O_3–13wt.% TiO_2 ceramic coatings were fabricated on austenitic SS which improved its hydrogen permeation resistance having extensive application in petroleum and chemical engineering industries [138]. Q235 steel coated with Al_2O_3–13 wt.% TiO2 was found to have superior corrosion resistance having potential application in power transmission systems and the marine industry [139]. 316L austenitic steel coated with Al_2O_3 had improved corrosion resistance in high-temperature atmospheres, which can be of greater help in boilers, furnaces, and nuclear installations [140]. SS304 coated with Al_2O_3-40 wt.% TiO_2 had improved wear resistance which points out the potential applications in thermal power plants and textile industries [141]. The SHS C-T process is a useful method for creating composite pipes with ceramic lining that solves drawbacks of several existing methods such as thin ceramic layer thickness (1 mm), inferior interface bonding, and high investment. The products of these techniques have been widely used as conduits for coal slurry, oil, and cement industries [99].

4 Future Trends and Challenges

Even though various coatings had been reported using a wide variety of materials using various processes, there exists some analysis needed to be completed to get the required coatings with the desired properties. Changes in the duty cycle will have an impact on the way the pores develop and lead to connected pores transforming to isolated pores. The intensity of the spark discharge during the PEO process can be attributed to the various pore shapes of coatings, thus optimization of the process is to be considered for getting tailor-made properties and surface morphology [142]. Bioactive glass-based and silicate ceramic coatings

Table 2 SHS-CT process ceramic coating evaluation

SI No	SHS reaction	Particle Size	Additives	Pipe material	Properties	Ref.
1	$Fe_2O_3 + 2Al = Al_2O_3 + 2Fe \Delta H = 836KJ/mol$	Fe_2O_3 -16 µm Al—38 µm	–	Carbon steel pipe		[99]
2	$Fe_2O_3 + 2Al = Al_2O_3 + 2Fe \Delta H = 836KJ/mol$	Fe_2O_3 -50 µm Al—38 µm	SiO_2	N80 steel pipe	Fracture toughness—4.125 MPa $m^{1/2}$ compression-shear strength—30.9 MPa Microhardness—1566HV_1	[102]
3	$CrO_3 + 2Al = Al_2O_3 + Cr$	–	ZrO_2	Carbon steel pipes (C: 0.2wt %)	–	[103]
4	$Fe_2O_3 + 2Al = Al_2O_3 + 2Fe$ $CrO_3 + 2Al = Al_2O_3 + Cr$ $3Ti + B_4C = TiC + TiB_2$ $Ni + Fe = NiFe$ $Al + Fe = AlFe$	(Al, Ni, Fe_2O_3, CrO_3, B_4C, $Na_2B_4O_7$)—200 mesh Ti—250 mesh	$Na_2B_4O_7$	Hot rolled pipes (0.17%—C plain steel)	Microhardness—1300–1800 HV_1 Compressive strength—340-380 MPa	[104]
5	$Fe_2O_3 + 2Al = Al_2O_3 + 2Fe \Delta H = 836KJ/mol$ $Cr_2O_3 + 2Al = Al_2O_3 + 2Cr \Delta H = 530KJ/mol$ $CrO_3 + 2Al = Al_2O_3 + Cr \Delta H = 1094KJ$ $3NiO + 2Al = Al_2O_3 + 3Ni \Delta H = 928KJ/mol$	–	CaF_2	Low carbon steel pipe	Tensile strength—316 MPa	[107]
6	$Fe_2O_3 + 2Al = Al_2O_3 + 2Fe \Delta H = 836KJ/mol$ $Cr_2O_3 + 2Al = Al_2O_3 + 2Cr \Delta H = 530KJ/mol$ $3NiO + 2Al = Al_2O_3 + 3Ni \Delta H = 928KJ/mol$	Fe_2O_3 – 0.2–0.8 µm Cr_2O_3-0.5–2.0 µm Al-4-70 µm NiO-0.3 µm	SiO_2	Carbon steel Q235	Microhardness—2400HV Thermal shock resistance—10cycles	[108]
7	$Fe_2O_3 + 2Al = Al_2O_3 + 2Fe \Delta H = 836KJ/mol$ $Ti + C = TiC \Delta H = 183KJ/mol$	Fe_2O_3 < 5 µm Al < 75 µm Ti-100mesh C-100 mesh	–	Carbon steel pipe	Microhardness—2313HV	[109]
8	$Fe_2O_3 + 2Al = Al_2O_3 + 2Fe \Delta H = 836KJ/mol$	Fe_2O_3- 75–150 µm Al—75—150 µm	3 mol% Y_2O_3-doped ZrO_2	J55 steel pipe	Fracture toughness—5.74MPa$m^{1/2}$ Microhardness—1170HV Crushing strength—365 MPa	[110]
9	$4FeWO_4 + 12.667Al + B_2O_3 + X(Fe_2O_3 + 2Al) = 4Fe + 2W_2B + 6.333Al_2O_3 + X(Al_2O_3 + 2Fe)$	$FeWO_4$ < 70 µm Al < 50 µm B_2O_3 < 80 µm	Fe_2O_3	Low carbon steel pipe	Microhardness—1170HV	[124]

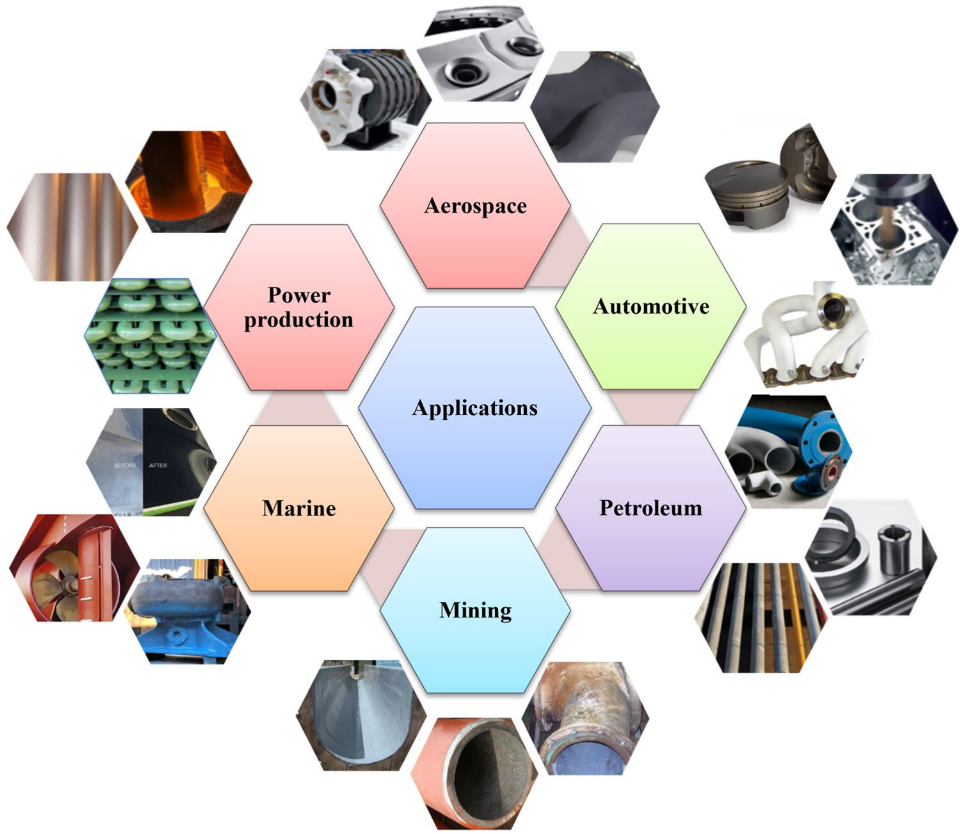

Fig. 12 Applications of ceramic coating in various fields

have shown promise as coating materials for orthopaedic and dental applications through mechanical and in-vitro biological investigations. The primary disadvantages associated with the usage of the earlier generations of hydroxyapatite implants appear to be resolved when new coatings are applied to metallic implants with sufficient adhesive properties to the substrates [143]. For both military and civilian purposes, the use of meta-surfaces to achieve the free regulation of electromagnetic wave scattering has attracted substantial recognition. Low dielectric CaO–B_2O_3–SiO_2 (CBS) glass–ceramic/Al_2O_3 composite coating processed by plasma spraying showed that an increase in CBS content effectively lowers the density and porosity. This enhances sintering densification which helps to be used for aircraft stealth applications and can be further explored for defence applications [144].

The coating microstructure being affected by particle properties, deposition temperature, and deposition had reduced impact due to accumulated stress and developed coating modulus. The stress developed during the deposition process and the deposition layer thickness are the crucial variables that determine the segmentation features of coating. Raising the deposition stress may reduce both the crack spacing and the thickness to cracking, although increased layer thickness by altering the parameters of the deposition process might increase the thickness of cracking, it can also result in smaller cracks [145]. The various qualities of coatings can be improved by adding additional feedstocks as seen in yttria and zirconia ceramic-reinforced WC–10Co4Cr cermet coatings. Additionally, there are not enough thorough investigations looking into the interfacial zone, micro/macro characteristics as well as tribo-mechanical properties of ceramic-reinforced cermet coatings [146]. Because of their lower dielectric constant, insulating properties at elevated temperatures, and superior thermal conductivity, the metallization of ceramics has grown to be a considerable factor for their application in the electronic sectors. In the temperature range of -60 to + 150 °C, Al_2O_3 and AlN ceramics with cold-sprayed Cu coatings could endure greater than 100 thermal cycles. By measuring the bonding strength of Al coatings on Al_2O_3 substrates, it was discovered that mechanical interlocking and heteroepitaxy bonding were key factors keeping Al coatings adhered to the ceramic surfaces. Understanding of the bonding mechanisms between metallic coatings and ceramics is still limited, hence more research with different materials and techniques needs to be done in order to advance the industry [147, 148].

Inefficient interfacial bonding that occurs between the lubricants and ceramics, along with mechanical property degradation brought on by tribological design, limit the practical applications of self-lubricating ceramic coatings. As a result, the first study with thermally sprayed ceramic coatings by creating crystalline–amorphous heterojunctions was conducted to address these issues. This prevents the mechanical property degradation of conventional ceramic self-lubricating coatings brought on by tribological design. Additional research is still required to fully explore the domain and its many potential practical applications [149]. The process of surface nanocrystallization produces a passive film at the nanometer scale, which reduces the corrosion current density and increases the corrosion potential and impedance. As a result, the material becomes more resistant to corrosion. This improved resistance is likely due to the refinement of the grain structure and the reduction in surface roughness achieved during the surface treatment [150]. The use of SMATed SS301 can provide superior protection against corrosion compared to untreated SS304 and SS316. This makes it a suitable substitute in manufacturing processes that require high resistance to corrosion. Furthermore, the environmental impact and potential harm to human health can be minimized since 301 SS contains fewer heavy metals such as Cr, Ni, and Co when compared to SS304 and SS316 [151]. Considering the perspectives of fuel loss and also radiological safety, tritium permeability in structural materials is a main concern in blanket systems of fusion reactors. The installation of a tritium permeation barrier (TPB) over components of metal pipes and blanket chassis is one of the technical approaches that helps in solving the issue. Various coating materials and procedures have been used to study ceramic coatings as TPBs, and they successfully reduced penetration. However, it is inevitable that liquid tritium breeders (Li–Pb alloy) will corrode the TPB. It is discovered that the coating deterioration occurs when Li–Pb is exposed to high temperatures. Additionally, as the number of ceramic surfaces increased, the coating deteriorates more severely during static Li–Pb exposure after the permeation test which revealed that in order to keep the ability of coatings to minimize permeability, fewer contacts between the various ceramics should be provided; more explorations are to be made to enhance the corrosion resistance of the TPBs [152].

5 Conclusions

The ceramic coating on steel refers to the application of a thin layer of ceramic material onto the surface of steel. This coating acts as a barrier that provides protection against wear, corrosion, and high temperature. The ceramic coating enhances the durability and longevity of the steel by reducing friction, improving thermal stability, and providing a smooth and hard surface. The application of ceramic coatings on steel is widely used in the automotive, aerospace, and industrial sectors. Ceramic coating over steel surface, properties, and applications have been reviewed in this work. Various methods of fabrication of coatings, significant process parameters, the influence of additives, metallurgical characterization, the effect of post-treatments are analysed. The corresponding improvements in the microstructures obtained, phases formed, and properties enhanced were evaluated. The microstructure of a ceramic coating is determined by several factors including the composition of the coating, the method of application, and the processing conditions. Typically, ceramic coatings have a homogeneous and dense microstructure with well-bonded ceramic particles. The size and distribution of the ceramic particles, as well as the presence of any porosity or defects, can greatly affect the performance of the coating. Ceramic coatings have proven to be a practical solution for improving functional properties like corrosion resistance, wear resistance, biocompatibility, anti-fouling, self-cleaning, and high-temperature stability. Numerous combinations of ceramic coatings over steel had already been produced but still there are numerous studies ongoing to optimize the parameters, enhance the properties, and to tailor make the coating for desired applications. Given the encouraging results, there is still a strong need to discover new composite ceramic coatings and improve their properties. Ceramic coatings can be utilized for highly advanced applications, such as fuel cells, nuclear power plants, and high-temperature applications.

Author Contributions N. Radhika: Conceptualization, Methodology, Supervision, Reviewing, and Editing. U.V. Akhil: Data curation, Writing—Original draft preparation, Visualization, and Investigation. L. Rajeshkumar: Reviewing and Editing. Giribaskar Sivaswamy: Reviewing and Editing. All authors read and approved the final manuscript.

Funding The authors declare that no funds, grants, or other support were received during the preparation of this manuscript.

Data Availability Not applicable.

Declarations

Competing interests The authors have no relevant financial or non-financial interests to disclose.

Ethical Approval Not applicable.

Consent to Participate Not applicable.

Consent for Publication Not applicable.

References

1. Matsumura M, Oka Y, Hiura H, Yano M (1991) The role of passivating film in preventing slurry erosion-corrosion of austenitic stainless steel. ISIJ Int 31:168–176. https://doi.org/10.2355/ISIJINTERNATIONAL.31.168
2. Nisar N, Bhat JA (2021) Effect of coupled deterioration mechanisms on corrosion of steel reinforcement: the role of chloride

ion ingress, freeze-thaw cycles and green corrosion inhibitor. J Bio Tribocorros 7:1–9. https://doi.org/10.1007/S40735-021-00564-X/METRICS
3. Modi OP, Dasgupta R, Prasad BK et al (2000) Erosion of a high-carbon steel in coal and bottom-ash slurries. J Mater Eng Perform 9:522–529. https://doi.org/10.1361/105994900770345647/METRICS
4. Cui L, Kang W, You H et al (2020) Experimental study on corrosion of J55 casing steel and N80 tubing steel in high pressure and high temperature Solution containing CO2 and NaCl. J Bio Tribo Corros. https://doi.org/10.1007/S40735-020-00449-5
5. Brownlie F, Hodgkiess T, Pearson A, Galloway AM (2021) A study on the erosion-corrosion behaviour of engineering materials used in the geothermal industry. Wear 477:203821. https://doi.org/10.1016/J.WEAR.2021.203821
6. Csaki loana, Manea CA, Trusca R, et al (2017) Microstructural Study of the Corrosion Effect on AlCrFeNiMn Multicomponent Alloy Tested in Geothermal Environment. Corros OnePetro
7. Taji I, Hoseinpoor M, Moayed MH, Pahlavan S (2020) Pitting corrosion of 17–4PH stainless steel: impingement of a fluid Jet vs. erosion-corrosion in the presence of the solid particles. J Bio Tribocorros 6:1–7. https://doi.org/10.1007/S40735-020-00428-W/METRICS
8. Handbook of Tribology: Materials, coatings, and surface treatments (Book) | OSTI.GOV. https://www.osti.gov/biblio/441774. Accessed 25 Jan 2023
9. Sam M, N R, Saleh B, (2022) Influence of boride, oxide, and carbide ceramics as secondary reinforcement in T6–A333 functionally graded hybrid composites. Ceram Int 48:28528–28547. https://doi.org/10.1016/J.CERAMINT.2022.06.167
10. Sam M, Radhika N (2022) Influence of carbide ceramic reinforcements in improving tribological properties of A333 graded hybrid composites. Defence Technology 18:1107–1123. https://doi.org/10.1016/J.DT.2021.06.005
11. Ibrahim KM, Havaldar SS, Hiriyannaiah A, Keshavamurthy R (2022) Investigation of corrosion characteristics of plasma-sprayed composite coating on bearing steel through electrochemical and salt spray test. J Bio Tribocorros 8:1–11. https://doi.org/10.1007/S40735-022-00706-9/METRICS
12. Farjami A, Yousefnia H, Seyedraoufi ZS, Shajari Y (2020) Investigation of Inhibitive Effects of 2-Mercaptobenzimidazole (2-MBI) and Polyethyleneimine (PEI) on Pitting Corrosion of Austenitic Stainless Steel. J Bio Tribocorros 6:1–19. https://doi.org/10.1007/S40735-020-00397-0/METRICS
13. DeMasi-Marcin JT, Gupta DK (1994) Protective coatings in the gas turbine engine. Surf Coat Technol 68–69:1–9. https://doi.org/10.1016/0257-8972(94)90129-5
14. Sreenivasulu V, Subramani P, Jayakumar V et al (2022) Development of protective coating for X8CrNiMoVNb16-13 alloy in high-temperature molten salt environment through high-velocity oxy-fuel sprayed NiCrMoNb and Cr_3C_2-25NiCr powder coating. Proc Inst Mech Eng Part E: J Process Mech Eng. https://doi.org/10.1177/09544089221115481/ASSET/IMAGES/LARGE/10.1177_09544089221115481-FIG8.JPEG
15. Kumar S, Bhaumik S, Patnaik L et al (2022) Application of integrated BWM Fuzzy-MARCOS approach for coating material selection in tooling industries. Materials 15:9002. https://doi.org/10.3390/MA15249002/S1
16. Dehghanghadikolaei A, Mohammadian B, Namdari N, Fotovvati B JOJ Material Sci Abrasive Machining Techniques for Biomedical Device Applications Doi: https://doi.org/10.19080/JOJMS.2018.04.555653
17. Fathi R, Wei H, Saleh B et al (2022) Past and present of functionally graded coatings: Advancements and future challenges. Appl Mater Today 26:101373. https://doi.org/10.1016/J.APMT.2022.101373
18. Saleh B, Ma A, Fathi R et al (2022) Wear characteristics of functionally graded composites synthesized from magnesium chips waste. Tribol Int 174:107692. https://doi.org/10.1016/J.TRIBOINT.2022.107692
19. Shen D, Li M, Gu W et al (2009) A novel method of preparation of metal ceramic coatings. J Mater Process Technol 209:2676–2680. https://doi.org/10.1016/J.JMATPROTEC.2008.06.017
20. Jojith R, Radhika N, Vigneshwar Raj R (2020) Characterization and wear behaviour of WC-Co coated copper under dry sliding conditions. Tribol Ind 42:327–336. https://doi.org/10.24874/TI.771.09.19.03
21. Jojith R, Radhika N (2021) Reciprocal dry sliding wear of SiCp/Al–7Si-0.3 Mg functionally graded composites: Influence of T6 treatment and process parameters. Ceram Int 47:30459–30470. https://doi.org/10.1016/J.CERAMINT.2021.07.225
22. Nachimuthu R, Sam M, Thangamayandi AR et al (2022) Tribological and mechanical characterization of as-cast and thermal treated Al-9Si/SiC graded composite. Proc Inst Mech Eng C J Mech Eng Sci 236:8092–8107. https://doi.org/10.1177/09544062221084189/ASSET/IMAGES/LARGE/10.1177_09544062221084189-FIG2.JPEG
23. Gowtham S, Arunnellaiappan T, Rameshbabu N (2016) An investigation on pulsed DC plasma electrolytic oxidation of cp-Ti and its corrosion behaviour in simulated body fluid. Surf Coat Technol 301:63–73. https://doi.org/10.1016/J.SURFCOAT.2016.02.043
24. Fattah-alhosseini A, Gashti SO, Molaie M (2018) Effects of disodium phosphate concentration (Na2HPO4·2H2O) on microstructure and corrosion resistance of plasma electrolytic oxidation (PEO) coatings on 2024 Al alloy. J Mater Eng Perform 27:825–834. https://doi.org/10.1007/S11665-018-3124-1/FIGURES/13
25. Molaei M, Babaei K, Fattah-alhosseini A (2021) Improving the wear resistance of plasma electrolytic oxidation (PEO) coatings applied on Mg and its alloys under the addition of nano- and micro-sized additives into the electrolytes: a review. J Magnes Alloy 9:1164–1186. https://doi.org/10.1016/J.JMA.2020.11.016
26. Yan Y, Han Y, Li D et al (2010) Effect of $NaAlO_2$ concentrations on microstructure and corrosion resistance of Al_2O_3/ZrO_2 coatings formed on zirconium by micro-arc oxidation. Appl Surf Sci 256:6359–6366. https://doi.org/10.1016/J.APSUSC.2010.04.017
27. Wang Y, Jiang Z, Yao Z, Tang H (2010) Microstructure and corrosion resistance of ceramic coating on carbon steel prepared by plasma electrolytic oxidation. Surf Coat Technol 204:1685–1688. https://doi.org/10.1016/J.SURFCOAT.2009.10.023
28. Zhao Z, Chen M, You C et al (2020) Effect of α-Al_2O_3 additive on the microstructure and properties of MAO coatings prepared on low carbon steel. J Market Res 9:3875–3884. https://doi.org/10.1016/J.JMRT.2020.02.014
29. Yang W, Li Q, Liu C et al (2017) A comparative study of characterisation of plasma electrolytic oxidation coatings on carbon steel prepared from aluminate and silicate electrolytes. Surf Eng 34:54–62. https://doi.org/10.1080/02670844.2017.1320862
30. Zhang G, Wu L, Tang A et al (2018) Electron beam surface alloying of carbon steel by aluminium followed by micro-arc oxidation. J Phys Conf Ser 1115:042065. https://doi.org/10.1088/1742-6596/1115/4/042065
31. Yu J, Zhang Y, Jin X et al (2019) Fabrication and optical emission spectroscopy of enhanced corrosion-resistant CPEO films on Q235 low carbon steel. Surf Coat Technol 363:411–418. https://doi.org/10.1016/J.SURFCOAT.2019.02.073
32. Malinovschi V, Marin A, Mihalache M, Iosub I (2016) Preparation and characterization of coatings on carbon steel obtained by PEO in silicate/carbonate electrolyte. Surf Coat Technol 296:96–103. https://doi.org/10.1016/J.SURFCOAT.2016.04.007
33. Yang W, Peng Z, Liu B et al (2018) Influence of silicate concentration in electrolyte on the growth and performance of plasma

electrolytic oxidation coatings prepared on low carbon steel. J Mater Eng Perform 27:2345–2353. https://doi.org/10.1007/S11665-018-3343-5/FIGURES/11

34. Li Y, Chen M, Li W et al (2019) Preparation, characteristics and corrosion properties of α-Al_2O_3 coatings on 10B21 carbon steel by micro-arc oxidation. Surf Coat Technol 358:637–645. https://doi.org/10.1016/J.SURFCOAT.2018.11.094
35. Huang M, Wang Y, Chu C, hui, et al (2017) Wear resistance of alumina-coated oil casing steel N80 via MAO with rare earth additive. Ceram Int 43:6397–6402. https://doi.org/10.1016/J.CERAMINT.2017.02.050
36. He X, Song RG, Kong DJ (2019) Microstructure and corrosion behaviours of composite coatings on S355 offshore steel prepared by laser cladding combined with micro-arc oxidation. Appl Surf Sci 497:143703. https://doi.org/10.1016/J.APSUSC.2019.143703
37. Zeng X, Zhang X, Pelenovich V et al (2023) High-temperature thin film lithium niobium oxide transducers for bolts. Ceram Int 49:7710–7716. https://doi.org/10.1016/J.CERAMINT.2022.10.262
38. Sirota V, Zaitsev S, Prokhorenkov D et al (2022) NiB-CrC coatings prepared by magnetron sputtering using composite ceramic NiCr-BC target produced by detonation spray coating. Nanomaterials 12:3584. https://doi.org/10.3390/NANO12203584
39. Lungu M, Cristea D, Baiasu F et al (2022) Surface, structural, and mechanical properties enhancement of Cr_2O_3 and SiO_2 co-deposited coatings with W or Be. Nanomaterials 12:2870. https://doi.org/10.3390/NANO12162870
40. Lyu L, Yang J, Zhou M et al (2023) Microstructure, mechanical properties and lead-bismuth eutectic corrosion behavior of (AlCrFeTiMo)NO and (AlCrFeTiNb)NO high entropy metal sublattice ceramic coatings. Vacuum 209:111774. https://doi.org/10.1016/J.VACUUM.2022.111774
41. Manninen NK, Calderón VS, Almeida Alves CF et al (2015) Influence of hydrogen incorporation and coating thickness on the corrosion resistance of carbon based coatings deposited by magnetron sputtering. Surf Coat Technol 275:127–132. https://doi.org/10.1016/J.SURFCOAT.2015.05.029
42. Olugbade TO, Abioye TE, Farayibi PK et al (2020) Electrochemical properties of MgZnCa-based thin film metallic glasses fabricated by magnetron sputtering deposition coated on a stainless steel substrate. Anal Lett 54:1588–1602. https://doi.org/10.1080/00032719.2020.1815757
43. Hu DC, Kuo DH, Kao JY et al (2023) Fabrication of nitride films by co-sputtering of high-entropy alloys and tungsten. J Aust Ceram Soc 59:105–115. https://doi.org/10.1007/S41779-022-00816-0/METRICS
44. de Castilho BCNM, de Sousa MF, Rodrigues AM et al (2022) Tailoring the hybrid magnetron sputtering process (HiPIMS and dcMS) to manufacture ceramic multilayers: powering conditions, target materials, and base layers. Nanomaterials 12:2465. https://doi.org/10.3390/nano12142465
45. Schmid B, Koutná N, Hahn R et al (2023) Development of TaC-based transition metal carbide superlattices via compound target magnetron sputtering. Int J Refract Metals Hard Mater 113:106165. https://doi.org/10.1016/J.IJRMHM.2023.106165
46. He CY, Zhao P, Gao XH et al (2022) High-entropy alloy nitride nanofilms via a co-sputtering method enable superior optical performance and thermal robustness. Mater Lett 329:133198. https://doi.org/10.1016/J.MATLET.2022.133198
47. Chen T, Wu W, Li W, Liu D (2019) Laser cladding of nanoparticle TiC ceramic powder: effects of process parameters on the quality characteristics of the coatings and its prediction model. Opt Laser Technol 116:345–355. https://doi.org/10.1016/J.OPTLASTEC.2019.03.048
48. Chen H, Lu Y, Sun Y et al (2020) Coarse TiC particles reinforced H13 steel matrix composites produced by laser cladding. Surf Coat Technol 395:125867. https://doi.org/10.1016/J.SURFCOAT.2020.125867
49. Yu J, Ho H (2022) Microstructure and mechanical properties of (Ti, Nb)C ceramic-reinforced 316L stainless steel coating by laser cladding. Appl Sci 12:6684. https://doi.org/10.3390/APP12136684
50. Chen T, Li W, Liu D et al (2021) Effects of heat treatment on microstructure and mechanical properties of TiC/TiB composite bioinert ceramic coatings in-situ synthesized by laser cladding on Ti6Al4V. Ceram Int 47:755–768. https://doi.org/10.1016/J.CERAMINT.2020.08.186
51. Chen L, Zhao Y, Guan C, Yu T (2021) Effects of CeO_2 addition on microstructure and properties of ceramics reinforced Fe-based coatings by laser cladding. Int J Adv Manuf Technol 115:2581–2593. https://doi.org/10.1007/S00170-021-07297-8/FIGURES/13
52. Li Z, Wei M, Xiao K et al (2019) Microhardness and wear resistance of Al_2O_3-TiB_2-TiC ceramic coatings on carbon steel fabricated by laser cladding. Ceram Int 45:115–121. https://doi.org/10.1016/J.CERAMINT.2018.09.140
53. Zhu H, Ouyang M, Hu J et al (2021) Design and development of TiC-reinforced 410 martensitic stainless steel coatings fabricated by laser cladding. Ceram Int 47:12505–12513. https://doi.org/10.1016/J.CERAMINT.2021.01.108
54. Zhao Y, Yu T, Guan C et al (2019) Microstructure and friction coefficient of ceramic (TiC, TiN and B4C) reinforced Ni-based coating by laser cladding. Ceram Int 45:20824–20836. https://doi.org/10.1016/J.CERAMINT.2019.07.070
55. Li M, Han B, Wang Y et al (2016) Investigation on laser cladding high-hardness nano-ceramic coating assisted by ultrasonic vibration processing. Optik (Stuttg) 127:4596–4600. https://doi.org/10.1016/J.IJLEO.2016.01.194
56. Li M, Han B, Wang Y, Pu K (2017) Effects of La_2O_3 on the microstructure and property of laser cladding Ni-based ceramic coating. Optik (Stuttg) 130:1032–1037. https://doi.org/10.1016/J.IJLEO.2016.11.111
57. Zhang PX, Yan H, Sun YH (2021) Microstructure, microhardness and corrosion resistance of laser cladding Al_2O_3@Ni composite coating on 304 stainless steel. J Mater Sci 56:8209–8224. https://doi.org/10.1007/S10853-020-05741-W/FIGURES/14
58. Wu Q, Li W, Zhong N et al (2013) Microstructure and wear behavior of laser cladding VC–Cr_7C_3 ceramic coating on steel substrate. Mater Des 49:10–18. https://doi.org/10.1016/J.MATDES.2013.01.067
59. Zavareh MA, Sarhan AADM, Razak BBA, Basirun WJ (2014) Plasma thermal spray of ceramic oxide coating on carbon steel with enhanced wear and corrosion resistance for oil and gas applications. Ceram Int 40:14267–14277. https://doi.org/10.1016/J.CERAMINT.2014.06.017
60. Kang JJ, Xu BS, Wang HD, Wang CB (2014) Influence of contact stress on rolling contact fatigue of composite ceramic coatings plasma sprayed on a steel roller. Tribol Int 73:47–56. https://doi.org/10.1016/J.TRIBOINT.2013.12.019
61. Szkodo M, Bień A, Antoszkiewicz M (2016) Effect of plasma sprayed and laser re-melted Al_2O_3 coatings on hardness and wear properties of stainless steel. Ceram Int 42:11275–11284. https://doi.org/10.1016/J.CERAMINT.2016.04.044
62. Hospach A, Mauer G, Vaßen R, Stöver D (2012) Characteristics of ceramic coatings made by thin film low pressure plasma spraying (LPPS-TF). J Therm Spray Technol 21:435–440. https://doi.org/10.1007/S11666-012-9748-Z/FIGURES/7
63. Ghadami F, Ghadami S, Abdollah-Pour H (2013) Structural and oxidation behavior of atmospheric heat treated plasma

sprayed WC-Co coatings. Vacuum 94:64–68. https://doi.org/10.1016/J.VACUUM.2013.01.019
64. Praveen AS, Sarangan J, Suresh S, Siva Subramanian J (2015) Erosion wear behaviour of plasma sprayed NiCrSiB/Al_2O_3 composite coating. Int J Refract Metals Hard Mater 52:209–218. https://doi.org/10.1016/J.IJRMHM.2015.06.005
65. Shao F, Yang K, Zhao H et al (2015) Effects of inorganic sealant and brief heat treatments on corrosion behavior of plasma sprayed Cr_2O_3–Al_2O_3 composite ceramic coatings. Surf Coat Technol 276:8–15. https://doi.org/10.1016/J.SURFCOAT.2015.06.045
66. Thakare JG, Mulik RS, Mahapatra MM (2018) Effect of carbon nanotubes and aluminum oxide on the properties of a plasma sprayed thermal barrier coating. Ceram Int 44:438–451. https://doi.org/10.1016/J.CERAMINT.2017.09.196
67. Li Q, Song P, He X et al (2019) Plastic metallic-barrier layer for crack propagation within plasma-sprayed Cu/ceramic coatings. Surf Coat Technol 360:259–268. https://doi.org/10.1016/J.SURFCOAT.2018.12.124
68. Das P, Paul S, Bandyopadhyay PP (2018) Plasma sprayed diamond reinforced molybdenum coatings. J Alloys Compd 767:448–455. https://doi.org/10.1016/J.JALLCOM.2018.07.088
69. Qin Y, Jiao Q, Zheng G et al (2018) Effects of spray distance on the microstructure and mechanical properties of reactive plasma sprayed TiCN coatings. Ceram Int 44:17230–17239. https://doi.org/10.1016/J.CERAMINT.2018.06.181
70. Kalangi C, Bolleddu V, Allasi HL (2021) Tribological characteristics of carbon nanotubes-reinforced plasma-Sprayed Al_2O_3-TIO_2 Ceramic coatings. Adv Mater Sci Eng. https://doi.org/10.1155/2021/8094640
71. Ghara T, Bandyopadhyay PP (2022) Mechanical properties and residual Stress depth profiles of plasma sprayed ceramic coatings deposited under comparable particle temperature and velocity. J Therm Spray Technol 31:1889–1905. https://doi.org/10.1007/S11666-022-01412-1/FIGURES/9
72. Yao SW, Li CJ, Tian JJ et al (2016) Conditions and mechanisms for the bonding of a molten ceramic droplet to a substrate after high-speed impact. Acta Mater 119:9–25. https://doi.org/10.1016/J.ACTAMAT.2016.07.057
73. Li CJ, Luo XT, Yao SW et al (2022) The bonding formation during thermal spraying of ceramic coatings: a review. J Therm Spray Technol 31(4):780–817. https://doi.org/10.1007/S11666-022-01379-Z
74. Akhtari Zavareh M, Sarhan AADM, Karimzadeh R, Singh RSA, l K, (2018) Analysis of corrosion protection behavior of Al2O3-TiO2 oxide ceramic coating on carbon steel pipes for petroleum industry. Ceram Int 44:5967–5975. https://doi.org/10.1016/J.CERAMINT.2017.12.175
75. Govande AR, Chandak A, Sunil BR, Dumpala R (2022) Carbide-based thermal spray coatings: a review on performance characteristics and post-treatment. Int J Refract Metals Hard Mater 103:105772. https://doi.org/10.1016/J.IJRMHM.2021.105772
76. Pathak A, Sivakumar G, Prusty D et al (2015) Thermal spray coatings for blast furnace tuyere application. J Therm Spray Technol 24:1429–1440. https://doi.org/10.1007/S11666-015-0350-Z/FIGURES/11
77. Mubarok F, Armada S, Fagoaga I, Espallargas N (2013) Thermally sprayed SiC coatings for offshore wind turbine bearing applications. J Therm Spray Technol 22:1303–1309. https://doi.org/10.1007/S11666-013-9991-Y/FIGURES/8
78. Van Nguyen T, Nguyen TA, Le Thu Q, Pham Thi H (2019) Influence of plasma spraying parameters on microstructure and corrosion resistance of Cr3C2-25NiCr cermet carbide coating. Anti-Corros Methods Mater 66:336–342. https://doi.org/10.1108/ACMM-09-2018-2003/FULL/XML
79. Devarajan DK, Rangasamy B, Kirubaharan K, Mosas A (2023) State-of-the-art developments in advanced hard ceramic coatings using PVD techniques for high-temperature tribological applications. Ceramics 6:301–329. https://doi.org/10.3390/CERAMICS6010019
80. Lim KS, Kim YS, Hong SH et al (2020) Influence of N2 Gas flow ratio and working pressure on amorphous Mo–Si–N coating during magnetron sputtering. Coatings 10:34. https://doi.org/10.3390/COATINGS10010034
81. Abedi M, Abdollah-zadeh A, Vicenzo A et al (2019) A comparative study of the mechanical and tribological properties of PECVD single layer and compositionally graded TiSiCN coatings. Ceram Int 45:21200–21207. https://doi.org/10.1016/J.CERAMINT.2019.07.100
82. Wang WZ, Feng SS, Li ZM et al (2020) Microstructure and properties of micro-arc oxidation ceramic films on AerMet100 steel. J Market Res 9:6014–6027. https://doi.org/10.1016/J.JMRT.2020.04.005
83. Andrei VA, Coaca E, Ionita I et al (2017) Microstructures and micro composition developed by plasma electrolysis processing of 316L austenitic steels to obtain Al-containing surface layer. Mater Today Proc 4:6990–6999. https://doi.org/10.1016/J.MATPR.2017.07.029
84. Wang Y, Jiang Z, Yao Z (2009) Microstructure, bonding strength and thermal shock resistance of ceramic coatings on steels prepared by plasma electrolytic oxidation. Appl Surf Sci 256:650–656. https://doi.org/10.1016/J.APSUSC.2009.08.036
85. Microscopic and electrochemical characterization of alumina ceramic films developed onto 316l stainless steel by microarc oxidation in plasma electrolysis | Request PDF. https://www.researchgate.net/publication/323719852_Microscopic_and_electrochemical_characterization_of_alumina_ceramic_films_developed_onto_316l_stainless_steel_by_microarc_oxidation_in_plasma_electrolysis. Accessed 2 Feb 2023
86. Pezzato L, Settimi AG, Fanchin D et al (2022) Effect of Cu addition on the corrosion and antifouling properties of PEO coated Zinc-Aluminized steel. Materials 15:7895. https://doi.org/10.3390/MA15227895
87. Marple BR, Voyer J, Thibodeau M et al (2006) Hot corrosion of lanthanum zirconate and partially stabilized zirconia thermal barrier coatings. J Eng Gas Turbine Power 128:144–152. https://doi.org/10.1115/1.1924534
88. Liu Z, Yang H, Jia Y, Shu X (2017) Heat protective properties of NiCrAlY/Al2O3 gradient ceramic coating fabricated by plasma spraying and slurry spraying. Surf Coat Technol 327:1–8. https://doi.org/10.1016/J.SURFCOAT.2017.07.075
89. Han Y, guang, Yang Y, Wang L, et al (2018) Microstructure and properties of in-situ TiB2 matrix composite coatings prepared by plasma spraying. Appl Surf Sci 431:48–54. https://doi.org/10.1016/J.APSUSC.2017.04.107
90. An Y, Li S, Hou G et al (2017) Mechanical and tribological properties of nano/micro composite alumina coatings fabricated by atmospheric plasma spraying. Ceram Int 6:5319–5328. https://doi.org/10.1016/J.CERAMINT.2017.01.072
91. Hashemi SM, Parvin N, Valefi Z, Alishahi M (2019) Comparative study on tribological and corrosion protection properties of plasma sprayed Cr2O3-YSZ-SiC ceramic coatings. Ceram Int 45:21108–21119. https://doi.org/10.1016/J.CERAMINT.2019.07.087
92. Zhang M, Wang XH, Qu KL, Liu SS (2019) Effect of rare earth oxide on microstructure and high temperature oxidation properties of laser cladding coatings on 5CrNiMo die steel substrate. Opt Laser Technol 119:105597. https://doi.org/10.1016/J.OPTLASTEC.2019.105597
93. Qunshuang M, Yajiang L, Juan W, Kun L (2016) Microstructure evolution and growth control of ceramic particles in wide-band

laser clad Ni60/WC composite coatings. Mater Des 92:897–905. https://doi.org/10.1016/J.MATDES.2015.12.121
94. Liu J, Li Y, Tan N et al (2023) Microstructure and properties of the solid solution ceramic coating by high speed laser cladding. Opt Laser Technol 158:108792. https://doi.org/10.1016/J.OPTLASTEC.2022.108792
95. Zhang Z, Yu T, Kovacevic R (2017) Erosion and corrosion resistance of laser cladded AISI 420 stainless steel reinforced with VC. Appl Surf Sci 410:225–240. https://doi.org/10.1016/J.APSUSC.2017.03.137
96. Kumar DD, Kaliaraj GS, Kirubaharan AMK et al (2019) Biocorrosion and biological properties of sputtered ceramic carbide coatings for biomedical applications. Surf Coat Technol 374:569–578. https://doi.org/10.1016/J.SURFCOAT.2019.06.022
97. Miyazaki E, Odawara O (2001) Centrifugal-thermit process for production of composite pipes of various sizes. Process Centrifugation. https://doi.org/10.1007/978-1-4615-0687-4_28
98. Ikornikov DM, Andreev DE, Sanin VN, Yukhvid VI (2011) In-situ formation of cast granules in thermit-type shsreactions. Int J Self Propag High Temp Synth 20:15–19. https://doi.org/10.3103/S1061386211010079/METRICS
99. Li Y, Jiang L, Lu Q et al (2016) A study of ceramic-lined composite steel pipes prepared by shs centrifugal-thermite process. Sci Sintering 48(1):81–86
100. Odawara O (2007) Long ceramic-lined pipes with high resistance against corrosion, abrasion and thermal shock. Mater Manuf Process 8:203–218. https://doi.org/10.1080/10426919308934825
101. Mahmoodian R, Rahbari RG, Hamdi M (2011) Safety Issues Improvement in Ceramic Lined Composite Pipe Produced Using SHS Method. Proceeding of the 2nd International Conference on Industrial Engineering and Operations Management. https://doi.org/10.13140/2.1.3799.7769
102. Ye K, Li F, Zhang J et al (2021) Effect of SiO2 on microstructure and mechanical properties of composite ceramic coatings prepared by centrifugal-SHS process. Ceram Int 47:12833–12842. https://doi.org/10.1016/J.CERAMINT.2021.01.144
103. Yu GB, Tao FH, Wang SH et al (2014) Solidification behavior of lined Al_2O_3-ZrO_2 multiphase ceramics in SHS composite pipes. Adv Mat Res 905:109–112. https://doi.org/10.4028/WWW.SCIENTIFIC.NET/AMR.905.109
104. Meng QS, Chen SP, Zhao JF et al (2007) Microstructure and mechanical properties of multilayer-lined composite pipes prepared by SHS centrifugal-thermite process. Mater Sci Eng, A 456:332–336. https://doi.org/10.1016/J.MSEA.2006.12.016
105. Wang SX, Liang KM, Gu SR, Zhang XH (2001) Hercynite-free ceramic liner for composite steel pipe made using a self-propagating high-temperature synthesis gravitational-thermite process. J Am Ceram Soc 84:3043–3044. https://doi.org/10.1111/J.1151-2916.2001.TB01135.X
106. Miyazaki E, Odawara O (2003) Centrifugal effects on combustion synthesis of (Ti–B–C) compound system. Mater Res Bull 38:1375–1386. https://doi.org/10.1016/S0025-5408(03)00149-1
107. Wenjun X, Sheng Y, Shiju G, Hoyi L (2000) Stainless steel lined composite steel pipe prepared by centrifugal-SHS process. J Mater Sci 35:45–48. https://doi.org/10.1023/A:1004776112579/METRICS
108. Xue X-F, Wang Z-H, Zhou Z-H et al (2014) Bonding characteristics of the Al_2O_3-metal composite coating fabricated onto carbon steel by combustion synthesis. Int J Minerals Metall Mater. https://doi.org/10.1007/s12613-014-0985-7
109. Mahmoodian R, Hassan MA, Hamdi M et al (2014) In situ TiC–Fe–Al2O3–TiAl/Ti3Al composite coating processing using centrifugal assisted combustion synthesis. Compos B Eng 59:279–284. https://doi.org/10.1016/J.COMPOSITESB.2013.12.016
110. Xuan XH, Su ZG, Wen Z et al (2016) High-performance ceramic-Lined composite pipes with ZrO_2 additive prepared by centrifugal-SHS process. Mater Trans 57:573–581. https://doi.org/10.2320/MATERTRANS.MC201503
111. An J, Zhao J, Su ZG et al (2015) Microstructure and mechanical properties of ZTA ceramic-lined composite pipe prepared by centrifugal-SHS. Arab J Sci Eng 40:2701–2709. https://doi.org/10.1007/S13369-015-1747-1/METRICS
112. Le MT, Kim DJ, Lee JR et al (2008) Properties of ceramic layer formed by centrifugal thermit reaction with silicon sludge replacement. Mater Trans 49:1868–1873. https://doi.org/10.2320/MATERTRANS.MRA2008109
113. Mahmoodian R, Hassan MA, Rahbari RG et al (2013) A novel fabrication method for TiC-Al_2O_3-Fe functional material under centrifugal acceleration. Compos B Eng 50:187–192. https://doi.org/10.1016/j.compositesb.2013.02.016
114. Huang X, Zhang L, Zhao Z et al (2011) TiB2-(Ti, W)C eutectic composite ceramics prepared by combustion synthesis under high gravity. Adv Mat Res 177:386–389. https://doi.org/10.4028/WWW.SCIENTIFIC.NET/AMR.177.386
115. Xu B, Zhang L, Wang C, Duan R (2010) Investigation on Al_2O_3/YSZ eutectic ceramics lining in the pipes prepared by combustion synthesis. Adv Mat Res 105–106:12–15. https://doi.org/10.4028/WWW.SCIENTIFIC.NET/AMR.105-106.12
116. Licheri R, Orrù R, Cao G et al (2003) Self-propagating combustion synthesis and plasma spraying deposition of TiC–Fe powders. Ceram Int 29:519–526. https://doi.org/10.1016/S0272-8842(02)00196-7
117. Singsarothai S, Khanghamano M, Rachphet V, Niyomwas S (2016) Influence of CaO_2 additives on the properties of Fe–WB-based composite lining deposited by centrifugal SHS on the inner surface of steel pipe. Int J Self Propag High Temp Synth 25:181–185. https://doi.org/10.3103/S1061386216030110/METRICS
118. An J, Yan X, Lv X, Wen Z (2017) Microstructure, mechanical properties and corrosion of ceramic-lined composite steel pipe prepared by centrifugal-SHS process. Sci Sinter 49:359–372. https://doi.org/10.2298/SOS1704359A
119. Andreev DE, Sanin VN, Sachkova N, v., Yukhvid VI, (2011) Cermet-lined tubes from industrial wastes by centrifugal SHS. Int J Self Propag High Temp Synth 20:27–32. https://doi.org/10.3103/S106138621101002X/METRICS
120. Lee J, Le MT, Chung HS (2007) Physical properties of ceramic layer prepared by SHS in centrifugal field. Mater Trans 48:2960–2963. https://doi.org/10.2320/MATERTRANS.MRA2007617
121. Huang X, Zhang L, Zhao Z, Yin C (2011) Preparation and properties of solidified TiC-TiB2 with hypoeutectic, eutectic and hypereutectic microstructures. Adv Mat Res 233–235:999–1004. https://doi.org/10.4028/WWW.SCIENTIFIC.NET/AMR.233-235.999
122. Ma T, Zhao Z, Zhang L et al (2011) High-hardness solidified TiB2-TiC composites prepared by combustion synthesis under high gravity. Adv Mat Res 233–235:1734–1739. https://doi.org/10.4028/WWW.SCIENTIFIC.NET/AMR.233-235.1734
123. Wang YF, Yang ZG (2007) Finite element analysis of residual thermal stress in ceramic-lined composite pipe prepared by centrifugal-SHS. Mater Sci Eng, A 460–461:130–134. https://doi.org/10.1016/J.MSEA.2007.01.017
124. Singsarothai S, Rachphet V, Niyomwas S (2016) Steel pipe-lined Fe-W2B-based composite coating by centrifugal-Self-propagating high-temperature synthesis process. J Ceram Soc Jpn 124:1123–1126. https://doi.org/10.2109/JCERSJ2.16122
125. Xue D, Mihaylova Y (2005) Current and future applications of surface engineering. Eng J 59:287–292
126. Fagoaga I, Viviente JL, Gavin P et al (1998) Multilayer coatings by continuous detonation system spray technique. Thin Solid

Films 317:259–265. https://doi.org/10.1016/S0040-6090(97)00524-5
127. Tailor S, Mohanty RM, Sharma VK, Soni PR (2014) Fabrication and wear behavior of nanostructured plasma-sprayed 6061Al-SiCp composite coating. J Therm Spray Technol 23:1081–1088. https://doi.org/10.1007/S11666-014-0065-6/FIGURES/9
128. Bhatia R, Sidhu HS, Sidhu BS (2015) High temperature behavior of Cr_3C_2-NiCr coatings in the actual coal-fired boiler environment. Metall Mater Trans E 2:70–86. https://doi.org/10.1007/S40553-015-0045-X
129. Swain B, Patel S, Mallick P, et al Solid particle erosion wear of plasma sprayed NiTi alloy used for aerospace applications
130. Jasempoor F, Elmkhah H, Imantalab O, Fattah-alhosseini A (2022) Improving the mechanical, tribological, and electrochemical behavior of AISI 304 stainless steel by applying CrN single layer and Cr/CrN multilayer coatings. Wear. https://doi.org/10.1016/J.WEAR.2022.204425
131. (PDF) Wear Behavior of plasma sprayed 8YSZ Thermal Barrier Coating on Stainless steel Substrate. https://www.researchgate.net/publication/306405752_Wear_Behavior_of_plasma_sprayed_8YSZ_Thermal_Barrier_Coating_on_Stainless_steel_Substrate. Accessed 2 Feb 2023
132. Zavareh MA, Sarhan AADM, Zavareh PA et al (2016) Development and protection evaluation of two new, advanced ceramic composite thermal spray coatings, Al_2O_3-40TiO_2 and Cr_3C_2-20NiCr on carbon steel petroleum oil piping. Ceram Int 42:5203–5210. https://doi.org/10.1016/J.CERAMINT.2015.12.044
133. Kawahara Y (2016) An overview on corrosion-resistant coating technologies in biomass/waste-to-energy plants in recent decades. Coatings 6:34. https://doi.org/10.3390/COATINGS6030034
134. Bolelli G, Berger LM, Bonetti M, Lusvarghi L (2014) Comparative study of the dry sliding wear behaviour of HVOF-sprayed WC–(W, Cr)2C–Ni and WC–CoCr hardmetal coatings. Wear 309:96–111. https://doi.org/10.1016/J.WEAR.2013.11.001
135. Hoyt KO, Gannon PE, White P et al (2012) Oxidation behavior of $(Co, Mn)_3O_4$ coatings on preoxidized stainless steel for solid oxide fuel cell interconnects. Int J Hydrogen Energy 37:518–529. https://doi.org/10.1016/J.IJHYDENE.2011.09.028
136. Salman S, Köse R, Urtekin L, Findik F (2006) An investigation of different ceramic coating thermal properties. Mater Des 27:585–590. https://doi.org/10.1016/J.MATDES.2004.12.010
137. Olugbade T, Lu J (2019) Enhanced corrosion properties of nanostructured 316 stainless steel in 0.6 M NaCl solution. J Bio Tribocorros 5:1–11. https://doi.org/10.1007/S40735-019-0235-7/METRICS
138. Song RG (2003) Hydrogen permeation resistance of plasma-sprayed Al_2O_3 and Al_2O_3-13wt.% TiO_2 ceramic coatings on austenitic stainless steel. Surf Coat Technol 168:191–194. https://doi.org/10.1016/S0257-8972(03)00002-1
139. Zhou J, Sun K, Huang S et al (2020) Fabrication and property evaluation of the Al_2O_3-TiO_2 composite coatings prepared by plasma spray. Coatings 10:1–15. https://doi.org/10.3390/COATINGS10111122
140. Andrei VA, Radulescu C, Malinovschi V et al (2020) Aluminum oxide ceramic coatings on 316l austenitic steel obtained by plasma electrolysis oxidation using a pulsed unipolar power supply. Coatings 10:318. https://doi.org/10.3390/COATINGS10040318
141. Kumar D, Murtaza Q, Walia RS, Singh P (2022) Comparative investigation on thermally sprayed Al_2O_3, Al_2O_3–13%(TiO2) and Al_2O_3–40%(TiO_2) composite coatings from room to 400 °C temperature. Surf Topogr 10:015043. https://doi.org/10.1088/2051-672X/AC5A75
142. Tuo Y, Yang Z, Guo Z et al (2023) Pore structure optimization of MoS2/Al2O3 self-lubricating ceramic coating for improving corrosion resistance. Vacuum 207:111687. https://doi.org/10.1016/J.VACUUM.2022.111687
143. Brunello G, Elsayed H, Biasetto L (2019) Bioactive glass and silicate-based ceramic coatings on metallic implants: open challenge or outdated topic? Materials. https://doi.org/10.3390/MA12182929
144. Li Q, Xie J, Hu J et al (2022) Influence of Ca/Al ratio on physical and dielectric properties of Al_2O_3/CaO-B_2O_3-SiO_2 glass-ceramics composite coatings prepared by high enthalpy atmospheric plasma spraying. J Eur Ceram Soc 42:1501–1509. https://doi.org/10.1016/J.JEURCERAMSOC.2021.11.021
145. Shinde S, v., Sampath S, (2022) Factors governing segmentation crack characteristics in air plasma sprayed ceramics. J Eur Ceram Soc 42:1077–1087. https://doi.org/10.1016/J.JEURCERAMSOC.2021.10.064
146. Singh J, Kumar S, Mohapatra SK (2019) Tribological performance of Yttrium (III) and Zirconium (IV) ceramics reinforced WC–10Co4Cr cermet powder HVOF thermally sprayed on X2CrNiMo-17-12-2 steel. Ceram Int 45:23126–23142. https://doi.org/10.1016/J.CERAMINT.2019.08.007
147. Kosarev VF, Klinkov S, v., Melamed BM, et al (2018) Cold spraying for power electronics: Deposition of thick topologically patterned copper layers on ceramics. AIP Conf Proc 2027:030047. https://doi.org/10.1063/1.5065141
148. Qin J, Huang Q, Wang X et al (2021) Interfacial metal/ceramic bonding mechanism for metallization of ceramics via cold spraying. J Mater Process Technol 288:116845. https://doi.org/10.1016/J.JMATPROTEC.2020.116845
149. Li S, Yu C, Deng C et al (2022) Optimized mechanical and tribological properties of thermally sprayed ceramic coatings by constructing crystalline–amorphous heterojunctions. Appl Surf Sci 604:154552. https://doi.org/10.1016/J.APSUSC.2022.154552
150. Olugbade TO, Omiyale BO, Ojo OT (2021) Corrosion, corrosion fatigue, and protection of magnesium alloys: mechanisms, measurements, and mitigation. J Mater Eng Perform 31(3):1707–1727. https://doi.org/10.1007/S11665-021-06355-2
151. Olugbade T, Liu C, Lu J (2019) Enhanced Passivation Layer by Cr Diffusion of 301 Stainless Steel Facilitated by SMAT. Adv Eng Mater 21:1900125. https://doi.org/10.1002/ADEM.201900125
152. Akahoshi E, Matsunaga M, Kimura K et al (2021) Deuterium permeation through multi-layer ceramic coatings under liquid lithium-lead exposure condition. Corros Sci 189:109583. https://doi.org/10.1016/J.CORSCI.2021.109583